Available online at www.sciencedirect.com
SCIENCE DIRECT®
Spectrochimica Acta Part B 58 (2003) 1867–1893
SPECTROCHIMICA ACTA PART B
www.elsevier.com/locate/sab

# Laser ablation for analytical sampling: what can we learn from modeling?

Annemie Bogaerts[a,*], Zhaoyang Chen[a], Renaat Gijbels[a], Akos Vertes[b]

[a]*University of Antwerp, Department of Chemistry, Universiteitsplein 1, Wilrijk-Antwerp, B-2610, Belgium*
[b]*George Washington University, Deparment of Chemistry, Washington, DC 20052, USA*

Received 4 July 2003; accepted 22 August 2003

**Abstract**

The paper is built up in two parts. First, a rather comprehensive introduction is given, with a brief overview of the different application fields of laser ablation, focusing mainly on the analytical applications, and an overview of the different modeling approaches available for laser ablation. Further, a discussion is presented here about the laser evaporated plume expansion in vacuum or in a background gas, as well as about the different mechanisms for particle formation in the laser ablation process, which is most relevant for laser ablation as solid sampling technique for inductively coupled plasma (ICP) spectrometry. In the second part, a model is presented that describes the interaction of an ns-pulsed laser with a Cu target, as well as the resulting plume expansion and plasma formation. The results presented here, include the temperature distribution in the target, the melting and evaporation of the target, the vapor density, velocity and temperature distribution in the evaporated plume, the ionization degree and the density profiles of $Cu^0$ atoms, $Cu^+$ and $Cu^{2+}$ ions and electrons in the plume (plasma), as well as the resulting plasma shielding of the incoming laser beam. Results are presented as a function of time during and after the laser pulse, and as a function of position in the target or in the plume. The influence of the target reflection coefficient on the above calculation results is investigated. Finally, the effect of the laser pulse fluence on the target heating, melting and vaporization, and on the plume characteristics and plasma formation is studied. Our modeling results are in reasonable agreement with calculated and measured data from literature.


*Keywords:* Laser ablation; Modeling; Evaporation; Plume expansion; Plasma; Inductively coupled plasma

## 1. Introduction

### *1.1. Laser ablation application fields*

Laser ablation (LA) is used for a growing number of applications, such as pulsed laser deposition [1–3], nanoparticle manufacturing [4], micromachining [5,6], surgery [7], as well as chemical analysis [8–10]. Several analytical techniques make use of the mechanism of laser–solid interaction, in different regimes of laser irradiance, including, among others, matrix assisted laser desorption ionization (MALDI) [11], laser microprobe mass spectrometry (LMMS) [12], laser-induced breakdown spectrometry (LIBS) [13].

*Corresponding author. Tel.: +3238202377; fax: +3238202376.
*E-mail address:* annemie.bogaerts@ua.ac.be (A. Bogaerts).

0584-8547/03/$ - see front matter © 2003 Elsevier B.V. All rights reserved.
doi:10.1016/j.sab.2003.08.004

Last but not least, in inductively coupled plasma mass spectrometry and optical emission spectrometry (LA-ICP-MS and LA-ICP-OES), laser ablation is used as solid sample introduction method [14–20]. In spite of the many applications, the exact mechanisms of laser ablation (e.g. thermal vs. mechanical effects, mechanisms of particle formation,…) are not yet fully understood. Moreover, different kinds of mechanisms can play a role, depending on the type of material, the laser irradiance, the laser pulse length, etc. In particular, LA-ICP-MS, which is today's most suitable technique for direct solid analysis, is still suffering from a number of drawbacks, which are related to the ablation process, the aerosol transport and the vaporization, atomization and ionization of the laser-induced product within the ICP. A number of experimentally gained insights into the fundamental processes demonstrate the need of models helping to localize such drawbacks and to define regimes where these problems can be minimized or overcome.

Therefore, we try to develop a numerical model, describing the various processes related to the laser-solid interaction, as well as the behavior of the laser-ablated material. As a first step, we would like to describe the most important parameters to improve the technique in general. We will focus in first instance on the application of nanosecond laser ablation of metals, as sample introduction technique for the ICP, to define the ablation process and to gain further insights into which part of the sample is removed, converted into atoms and ions, and to describe its expansion dimensions above the sample surface. Further studies and models will incorporate the ablation cell, gas flows, aerosol transport and ICP conditions. At this stage, however, the model will also be useful for other applications, operating at similar conditions.

### *1.2. Overview of different modeling approaches for LA*

In the literature, a variety of models for laser ablation are available, operating in different regimes of wavelength (UV, Vis, IR), laser irradiance ($10^4$–$10^{10}$ W/cm$^2$), pulse length (fs, ps, ns), target material (metals, organic solids, …), gas environment (vacuum, ambient gas), and applied to the various applications mentioned above. A large number of models for laser–solid interaction are based on thermal processes: heating of the solid, followed by melting and evaporation. They describe the laser–solid interaction on a macroscopic scale, i.e. by the thermal heat conduction equation [21–38]. This assumption is justified for ns-pulsed laser interaction, especially for metals. Indeed, in metals, light is absorbed by interaction with electrons. A quantum of optical energy is absorbed by an electron, which is raised to a higher energy state in the conduction band. The excited electrons collide with lattice phonons, thereby transferring the absorbed energy to the lattice. Since the energy relaxation time is of the order of $10^{-13}$ s for metals [1,39], the optical energy can be regarded as being instantaneously turned into heat for ns-pulsed laser ablation. Therefore, the concepts of temperature and heat conduction are applicable [39]. For ps-pulsed and fs-pulsed lasers, the electron energy cannot be regarded as instantaneously turned into heat, and a two-temperature model is needed, which describes the coupling of the electron temperature and the lattice temperature [40–47]. Further, there exist also a few kinds of microscopic models, based on the Boltzmann transport equation for transport of electrons and for electron–lattice interactions [48], or based on molecular dynamics simulations, for metals [49,50] or for organic solids [51–55]. However, these models are limited to a short time-scale, because of the long computation time. A mesoscopic model [56–59] provides a link between the microscopic and macroscopic phenomena. The time-scale is less limited than in molecular dynamics simulations, and the highly non-equilibrium behavior can be adequately described. Finally, a number of analytical models for laser ablation have been reported [60–66].

Several models do not only focus on the laser–solid interaction, but they describe also the expansion of the evaporated material plume, or they concentrate solely on the expansion process, assuming certain input from the evaporated material. The plume expansion can be investigated either by hydrodynamic models [25–38,67–81],

by Monte Carlo simulations [82–92], or by a combination of both [93,94]. Most of the hydrodynamic models for plume expansion also consider the formation of a plasma of the evaporated material [29–38,67–74,76,77]. A few models focus mainly on the plasma, either from the evaporated material [66,95,96], or the early-stage plasma due to electron emission from the target [97–99], because this plasma can absorb a fraction of the incoming laser intensity before it reaches the target (so-called 'plasma-shielding').

### *1.3. Laser-evaporated plume expansion in vacuum or in a background gas*

Nearly all models describing laser–solid interaction followed by plume expansion apply to expansion in vacuum or in a low pressure background gas (up till a few 100 Pa), which is easier to model (e.g. only one type of material to follow, and no interactions with the surrounding gas), and which is close to reality for many applications (e.g. pulsed laser deposition). Some papers have investigated the effect of background gas on the plume expansion with hydrodynamic models [27–32,69–81], but the pressure is mostly limited till approximately 100 Pa or lower [30–32,69–75], with a few exceptions till 1 atm [27–29,76–81]. The general effect of the background gas is reported to be the spatial confinement and slowing down of the expanding plume. Moreover, the material can even move backward, and several reflected shocks within the plume were observed [31]. In most of the papers investigating the effect of the background gas, no additional conservation equations (for the background gas) or extra terms in the equations for the material plume (describing interactions with the background gas) are presented. This would, however, be necessary for a realistic description of the behavior of the expanding plume in a background gas, especially at atmospheric pressure. Wood et al. have included some scattering terms in the hydrodynamics equations, to account for the transfer of momentum from the plume to the background gas [72–74], but the model is only applied to low pressure (below 50 Pa). Gnedovets et al. have reported a hydrodynamic model with two distinct species (material plume and background gas) and interactions between them [78–80]. This model is applied to expansion in a background gas at 1 atm, but for a long laser pulse (ms-range) at very low laser irradiance ($10^4$–$10^5$ W/cm$^2$), so that no plasma is formed. A similar model was, however, also applied recently to higher laser irradiance, but again with the assumption of no plasma formation [81]. Finally, the effect of the background gas is also investigated in several Monte Carlo simulations [88–92] or combined hydrodynamic—Monte Carlo models [93,94], but they are again only applied to pressures below a few 100 Pa.

However, when laser ablation is used as sample introduction technique for the ICP, the ablation cell is filled with a gas (typically helium or argon) at 1 atm, and this gas is used to transfer the ablated material to the ICP (e.g. Ref. [16]). Also, in LIBS, the laser ablation typically takes place at 1 atm [76,96,100], although a wide pressure range ($10^{-5}$–1 atm) is also possible [100,101]. It is reported from experiments [102] that the expansion dynamics of the evaporated plume is highly dependent on the background gas pressure. Free expansion, plume splitting and sharpening, hydrodynamic instability and stagnation of the plume were observed at different pressure levels between $10^{-6}$ and 100 Torr [102]. Other experiments have revealed that the gas medium significantly affects the laser ablation efficiency [103,104]. Indeed, the ICP emission intensity increases when using a background gas with a higher ionization potential (e.g. He), due to less plasma shielding, and hence, more efficient laser sampling [103,104]. Therefore, the effect of the background gas should in principle be incorporated for realistic modeling of the laser ablation process.

### *1.4. Particle formation in the LA process*

It is generally known that the laser ablated material consists not only of evaporated atoms, but particles are also formed, either directly by the laser–solid interaction, or later, through condensation in the expanding plume (see below). These particles are the subject of many methodological investigations in LA-ICP-MS and LA-ICP-OES, because they are considered to be the main source

of elemental fractionation (i.e. non-stoichiometric ablation: the analytical signal does not represent exactly the sample composition) [20,105–110]. Elemental (or isotopic) fractionation may occur during the ablation process (e.g. preferential volatilization of lighter elements (or isotopes), perhaps coupled with preferential condensation), during the aerosol transport (e.g. preferential transport of smaller particles), as well as in the ICP, i.e. due to incomplete vaporization (atomization, ionization, excitation) of the aerosol. Whereas over the past 17 years, the laser–sample interaction was considered to be the major source of fractionation, nowadays, aerosol transport, and especially the ICP are believed to have an important effect as well [20,110]. Recent studies have proven that the aerosol structure, i.e. the particle size distribution, has significant effect on elemental fractionation [20,106–110]. The laser produced aerosol can be subdivided into three fractions: (a) the largest particles are too heavy to be transported; (b) the particles with intermediate size can be transported to the ICP, but cannot completely be vaporized; and (c) the fraction consisting of vapor and small particles can be completely transported and vaporized in the ICP. The degree of elemental fractionation will depend on the ratio of these three fractions. If the majority of particles are small enough, elemental fractionation will not be significant. However, if the fraction of larger particles increases, an increasing number of particles will not be transported or fully vaporized, and elemental fractionation becomes increasingly important. Therefore, controlling the particle size distribution is of uttermost importance [108,109].

In spite of the large variety of models available for laser ablation (see above), not many do consider the formation of particles. Nevertheless, particle formation is not only important for LA as sample introduction technique for the ICP, but it has also major consequences in the other application fields of laser ablation. Indeed, the particles present in the vapor plume scatter the incident laser light, which leads to a shielding of the target surface [77,111]. Further, the quality of microstructures manufactured by laser ablation can be considerably reduced due to the formation of debris in the surrounding area, as a result of the presence of nanoparticles [77]. However, nanoparticle synthesis is also a promising application of laser ablation [78,112–116].

A number of models describe particle formation and growth in the expanding vapor plume, based on condensation and nucleation theories [38,77] or effusion theory [111]. Using simple formulas, information is obtained about particle size distribution and rate of cluster growth. A one-dimensional particle formation model, based on condensation and nucleation theory, is developed by Gnedovets et al. [78–80] and Blair et al. [81], and it is coupled to the expansion dynamics of the evaporating plume and the background gas, assuming no plasma formation. This model is applied to laser ablation in 1 atm background gas. Indeed, Wood et al. suggest that the background gas plays a dominant role in particle formation [74]. Han et al. drew similar conclusions, because the cluster formation efficiency is determined by the rate of collisions between clusters, vapor atoms and background gas, which is controlled by the density of vapor atoms and buffer gas atoms [92]. It is suggested that shock wave formation and reflection phenomena due to the buffer gas play an important role in the nanoparticle formation [92]. Zhigilei also states that efficient particle formation is expected when the background gas pressure is sufficiently high, so that many collisions of the vapor species can occur, although condensation can take place under vacuum conditions as well [117]. In general, condensation droplets are typically formed in long-pulse (ms) and low-intensity ($10^4$–$10^5$ W/cm$^2$) regimes [78]; however, they can also be generated at higher laser intensity and shorter pulse (e.g. $10^8$–$10^{10}$ W/cm$^2$ and few ns pulse) under slow expansion of the vapor plume into the background gas [118].

The average particle size predicted with the above models, ranges from approximately 1 nm [81] to tens [38,77] and even a few hundred nanometers [38,78,79], depending on the applied theory and the conditions. Normally, condensation is used to explain the observation of small particles, composed of tens to thousands of atoms/molecules. Formation of larger (sub-micrometer and micrometer sized) particles would require an unrealistically high number of collisions to occur

in the expanding plume. Therefore, the larger particles are probably the result of direct ejection from the target [117,118].

Different mechanisms can play a role for direct cluster ejection from the target, depending on the target material. The ejection of large liquid droplets and/or solid particulates can be caused by photomechanical effects, as a result of laser-induced stress [117]. When the laser-induced stresses exceed the dynamic tensile strength of the target material, i.e. in the regime of stress confinement, when the laser pulse duration is shorter than the time needed for mechanical equilibration, cavitation and disruption of a liquid surface region, or mechanical fracture/spallation of a solid target can take place [53–55,117,119,120]. The importance of this mechanism depends on the mechanical properties of the target material, as well as the microstructure and surface roughness. This mechanism can probably play a significant role for organic materials (such as polymers) [53–55,117,119] as well as for geological materials (e.g. silicates) [121].

For metals, however, mechanical fragmentation is expected to be less important, and particles are assumed to be formed by liquid (large droplet) ejection, which can be the result of several processes, in general termed hydrodynamic sputtering [117]. Large droplets can be ejected as a result of a transient melting and motion of a liquid caused by steep gradients and the vapor plume recoil pressure [1,118,122,123]. The expulsion of melt by the impact of recoil pressure of the expanding vapor plume in a background gas is also called 'liquid splashing' [120]. This recoil pressure will be higher when the background gas is at higher pressure [123]. Due to this local pressure, surface hydrodynamic instabilities will be formed, which result in the ablation of liquid in the form of droplets [123]. The hydrodynamic mechanism of large droplet ejection in metals is strongly supported by the analysis of surface morphology [122,123]. Moreover, the splashing is expected to occur in the radial direction, which is confirmed by measured crater profiles [110].

At high laser irradiance, i.e. above $2.2\times10^{10}$ W/cm$^2$ in the case of silicon [124–126] and above $5\times10^{10}$ W/cm$^2$ for aluminum [127], or for short laser pulses [55,116], ejection of large particulates is found to be very important, and is attributed to phase explosion, or explosive boiling of the target material beneath the surface layer [124–127]. Indeed, bubbles are formed in this superheated liquid layer. Once these bubbles obtain a critical size, they can expand rapidly, initiating explosive boiling and mass ejection in the form of large (micrometer-sized) particulates [125,126]. Recently, evidence was found that explosive boiling occurs after completion of the laser pulse [126,127]. The importance of this mechanism at high laser irradiance is confirmed by the strong increase in crater volume and depth at a given threshold irradiance [124–126].

### *1.5. Present (basic) model for LA*

The above discussion shows that the entire process of laser ablation and the subsequent behavior of the ablated material (e.g. expansion into a background gas, plasma ignition, shock waves, particle formation,…) can be very complicated, and that it cannot readily be described with one single model. Therefore, it is our intention to describe the entire process step by step.

As a first step, we will describe in the present paper a model for the laser interaction of a copper target, yielding heating, melting and vaporization of the target material, followed by plume expansion, as well as plasma formation and shielding of the laser intensity. We will limit ourselves here to expansion in vacuum, so that only the evaporated material needs to be considered. Although this might not directly reflect the reality of laser ablation for the ICP, it is of interest to other applications (see above), and it can provide already some insight in the mechanisms. Moreover, preliminary calculations in our group have revealed that most of the modeling results are not fundamentally different for expansion in vacuum and in 1 atm background gas [128]. Also, particle formation will be neglected in this first step. This model will, however, serve as a basis for the later description of laser ablation in 1 atm helium or argon, and for the modeling of the formation and behavior of particles. However, even this basic model is

Table 1
Input data used in our model, for Cu as target material, as well as the references where the data are taken from. Some parameters, related to the target, are given both for solid and liquid (molten) phase, when the values are different

| Parameters | Values for Cu | Ref. |
|---|---|---|
| Thermal conductivity, $\kappa$ (W m$^{-1}$ K$^{-1}$) | 380 (solid), 170 (liquid) | [34] |
| Specific heat, $C_p$ (J kg$^{-1}$ K$^{-1}$) | 420 (solid), 494 (liquid) | [34] |
| Mass density, $\rho$ (kg m$^{-3}$) | 8960 (solid), 8000 (liquid) | [1,34] |
| Absorption coefficient, $\alpha$ (m$^{-1}$) | $7.44\times10^{7}$ | [34] |
| Reflectivity used in the model, $\Re$ | 0.34 | [95] |
| Melting point, $T_m$ (K) | 1358 | [1] |
| Boiling point, $T_b$ (K) | 2836 | [1] |
| Heat of fusion, $\Delta H_{sl}$ (J/mol) | $1.3\times10^{4}$ | [1] |
| Heat of vaporization, $\Delta H_{lv}$ (J/mol) | $3.048\times10^{5}$ | [1] |
| First ionization potential, $IP_1$ (eV) | 7.73 | [133] |
| Second ionization potential, $IP_2$ (eV) | 20.29 | [133] |
| Electronic work function, $\phi$ (eV) | 4.5 | [133] |

already quite complicated and considers already many processes.

Our modeling approach is based on a model that was actually developed more than a decade ago for another application, i.e. laser ablation microprobe mass analysis (LAMMA) [34]. It will be applied here to laser ablation conditions typical for LA-ICP-MS and LA-ICP-OES, and for LIBS, i.e. a laser pulse duration of several nanoseconds, and laser irradiance in the order of $10^9$ W/cm$^2$. Cu will be taken as the target material. In Section 2, the different aspects of the model will be outlined. Section 3 will show some typical results, for a copper target. The effect of target surface reflectivity and of laser intensity will be discussed in Sections 4 and 5, respectively. A comparison with other calculated or experimental results is made in Section 6. Finally, a conclusion and outlines for future work will be given in Section 7.

## 2. Description of the model

The model presented in this paper describes several mechanisms, related to the laser–solid interaction and the behavior of the evaporated material. The different parts of the model will be described in detail below, and the coupling between the various parts will be outlined.

### 2.1. Target heating, melting and vaporization

As a result of the laser impact onto the solid target, the temperature at the target surface will rise, and eventually, the target can melt, and even vaporize. The temperature distribution in the target is calculated with the heat conduction equation. The absorption length in the target ($l_{abs}=1/\alpha$ [1], with $\alpha$ defined as the absorption coefficient, $\alpha=7.44\times10^{7}$ m$^{-1}$; see Table 1) is in the order of 10 nm. Because this is much smaller than the laser beam diameter (typically in the order of 100 μm, e.g. [16]), the heat conduction can be solved in one dimension [22,24,28,39]:

$$\frac{\partial T(x,t)}{\partial t}=\frac{\partial}{\partial x}\left[\left(\frac{\kappa}{C_p\rho}\right)\frac{\partial T(x,t)}{\partial x}\right]+\frac{\alpha}{C_p\rho}\,I(x,t) \qquad (1)$$

where $T$ represents the temperature inside the target, $x$ is the position from the surface, $t$ is the time, $\kappa$, $C_p$, $\rho$ and $\alpha$ denote the thermal conductivity, heat capacity, mass density and absorption coefficient of the target material, respectively. The calculations are performed here for a Cu target, and the corresponding data used in the model, are summarized in Table 1. In the current model, non-linearities in material parameters, e.g. absorption coefficient, are neglected, and the thermal properties of the target material are assumed to be temperature-independent. This is not really true,

but for most metals the variations are relatively small over fairly wide temperature ranges [39].

The first term of the right-hand side represents the heat conduction, whereas the second term denotes the energy source by laser energy absorption. $I(x,t)$ stands for the laser irradiance as a function of time and position in the target, and can be written as:

$$I(x,t) = I_0(t)\exp(-\alpha x)[1-\Re] \quad (2)$$

$I_0(t)$ is the incident laser irradiance at the surface, and $\Re$ is the surface reflectivity. The latter is generally close to 1 for metals, but it can drop to values as low as 0.1 during laser ablation, when the irradiance is high enough (approx. $10^8$ W/cm$^2$) [1,39,122,129,130]. This is attributed to roughening due to the temperature increase of the surface, to removal of surface films, and to melting [39,122,129], although the details of the mechanism might not yet be fully understood [130]. We used a constant value of 0.34, as indicated in Table 1, because of lack of more accurate data, and in order not to further complicate the solution of the heat conduction equation. This is a reasonable intermediate value, which has also been reported in Ref. [95], albeit for a somewhat different wavelength, and it was not very clear where this value was adopted from. We have, however, investigated the effect of this parameter on the modeling results, as will be shown later in the paper, in Section 4.

When the temperature at a certain depth in the target exceeds the melting point of Cu, the target starts melting, and the local temperature remains constant during the time that phase transition takes place. Furthermore heating of the molten target is calculated in the same way, but using data for molten Cu (see Table 1). In the molten phase, convection is induced by the thermal gradient. Although this effect leads to additional heat transport, it is not part of the model. Melting normally starts at the surface, but the melt front (i.e. the interface between solid and molten phase) can extend inside the target when the temperature rises further. The heat conduction equation is solved as a function of time during and after the laser pulse, by an explicit finite difference method.

When the temperature at the surface becomes very high, vaporization becomes significant. The vapor pressure ($p_{\mathrm{vap}}$) is calculated from the surface temperature, by integrating the Clausius-Clapeyron equation [131]:

$$p_{\mathrm{vap}}(T_s) = p_0\exp\left[\frac{\Delta H_{\mathrm{lv}}(T_s - T_b)}{RT_sT_b}\right] \quad (3)$$

where $T_s$ and $T_b$ are the surface temperature and the normal boiling point at pressure $p_0 = 1$ atm, $\Delta H_{\mathrm{lv}}$ is the heat of vaporization, and $R$ is the gas constant. The data for a Cu target are also presented in Table 1.

From the vapor pressure, the vapor density at the surface ($\rho_{\mathrm{vap,s}}$) is calculated from the ideal gas law:

$$\rho_{\mathrm{vap},s} = \frac{p_{\mathrm{vap}}}{kT_s} \quad (4)$$

where $k$ is the Boltzmann constant.

Further, assuming that the vapor atoms leaving the surface follow a one-dimensional Maxwellian velocity distribution, the flow velocity of the vapor atoms above the surface ($v_{\mathrm{vap},s}$) can be approximated by the average of the normal velocity component at temperature $T_s$ [132]:

$$v_{\mathrm{vap},s} = \sqrt{\frac{2kT_s}{\pi m}} \quad (5)$$

where $m$ is the mass of a Cu atom.

The vapor density ($\rho_{\mathrm{vap},s}$), vapor velocity ($v_{\mathrm{vap},s}$) and vapor temperature at the surface ($T_s$) are used as input (i.e. boundary conditions) in the second part of the model.

### 2.2. Expansion of the evaporated material plume

The expansion of the evaporated material into vacuum is described by the Euler equations of hydrodynamics, expressing the conservation of mass density, momentum and energy [34]:

$$\frac{\partial \rho}{\partial t} = -\frac{\partial(\rho v)}{\partial x} \quad (6)$$

$$\frac{\partial(\rho v)}{\partial t} = -\frac{\partial}{\partial x}[p + \rho v^2] \tag{7}$$

$$\frac{\partial}{\partial t}\left[\rho\left(E + \frac{v^2}{2}\right)\right] = -\frac{\partial}{\partial x}\left[\rho v\left(E + \frac{p}{\rho} + \frac{v^2}{2}\right)\right] + \alpha_{IB} I_{laser} - \varepsilon_{rad} \tag{8}$$

Here $\rho$ is the mass density, $\rho v$ is the momentum, $\rho E$ is the internal energy density, $\rho v^2/2$ is the kinetic energy density, and $p$ is the local pressure. Assuming that the evaporated material follows the ideal gas law, the pressure and internal energy density can be expressed as Ref. [34]:

$$p = (1 + x_e)\frac{\rho kT}{m} \tag{9}$$

$$\rho E = \frac{\rho}{m}\left[\frac{3}{2}(1 + x_e)kT + IP_1 x_{i1} + (IP_1 + IP_2)x_{i2}\right] \tag{10}$$

Here, $x_e$, $x_{i1}$ and $x_{i2}$ stand for the fraction of electrons, singly charged ($Cu^+$) and doubly charged ($Cu^{2+}$) ions in the vapor, and $IP_1$ and $IP_2$ represent the first and second ionization potential of Cu (values taken from [133], see Table 1). These extra terms, and the factor $(1+x_e)$, are needed to account for the partial (or full) ionization of the vapor (see below). In this work, we assume that the Cu vapor can be ionized into both $Cu^+$ and $Cu^{2+}$ ions [34]. However, it is clear that this formula can be extended to higher charge multiplicity, when needed. In this formula, it is assumed that the electrons can be treated as ideal gas, following Maxwell–Boltzmann distribution.

Further, $I_{laser}$ is the laser irradiance and $\alpha_{IB}$ stands for the absorption coefficient due to inverse Bremsstrahlung, which is a function of position in the plume (see below). The product of $I_{laser}$ and $\alpha_{IB}$ gives the local laser energy absorption, which represents a gain for the internal energy of the vapor. Finally, $\varepsilon_{rad}$ is the amount of energy emitted by the vapor per unit volume and time in the Bremsstrahlung process, which means a loss for the internal energy of the vapor. Assuming that the electrons are characterized by a Maxwellian velocity distribution, $\varepsilon_{rad}$ can be expressed as [134]:

$$\varepsilon_{rad} = \left(\frac{2\pi kT}{3m_e}\right)^{1/2} \frac{32\pi e^6}{3hm_e c^3} n_e (Z_1^2 n_{i1} + Z_2^2 n_{i2}) \tag{11}$$

where $m_e$ and $e$ are the electron mass and charge, respectively, $c$ is the velocity of light, $n_e$, $n_{i1}$, $n_{i2}$ represent the densities of electrons, $Cu^+$ and $Cu^{2+}$ ions, and $Z_1$ and $Z_2$ stand for the charges of the singly and doubly charged ions ($Z_1 = 1$ and $Z_2 = 2$). Again, this formula can be extended if more multiply charged ionic species are present in the evaporated plume.

The second and third terms in the right-hand side of Eq. (8) represent non-linear terms, because they depend on the electron and ion densities, which in turn depend on the vapor density. Moreover, the vapor density can show large variations as a function of position, from near solid density till vacuum. This large discontinuity can give rise to shock waves. In order to accurately reflect this shock formation, an appropriate solution method needs to be used to solve the three conservation equations. We used a finite difference method, based on the first order Godunov scheme, which describes the shock wave as a series of analytically solvable mini-shocks (see Refs. [67,135–139] for more information). It is worth to mention that we have checked this Godunov solution method of the equations with another solution method, i.e. the second order MacCormack method (see, e.g. [139]), and both solution methods yielded the same results. The Godunov method was, however, preferred for the present application, because of the shorter computation time (i.e. ca. 5 times faster, mainly because a larger timestep could be used).

### *2.3. Plasma formation*

Because the temperature of the evaporated material is very high, the vapor is ionized (see above) and a plasma is formed. Since many collisions take place between the various particles, the plasma can be considered in local thermal equilibrium (LTE). This means that in a sufficiently small region of the plume, thermal equilibrium is established between the electrons, ions and neutrals,

and they are characterized with a common temperature. Moreover, the ionization degree (i.e. fraction of electrons and ions) can be described by the Saha–Eggert equation [9]. Because previous calculations have shown that not only $Cu^+$ ions, but also $Cu^{2+}$ ions are formed at the typical conditions under study here [34], two different Saha–Eggert equations are incorporated in the model, i.e. for the ratio of $Cu^+$ ions to $Cu^0$ atoms, and for the ratio of $Cu^{2+}$ to $Cu^+$ ions:

$$\frac{x_e x_{i1}}{x_0} = \frac{1}{n_{\text{vap}}}\left(\frac{2\pi m_e kT}{h^2}\right)^{3/2} \exp\left(-\frac{\text{IP}_1}{kT}\right) \tag{12}$$

$$\frac{x_e x_{i2}}{x_{i1}} = \frac{1}{n_{\text{vap}}}\left(\frac{2\pi m_e kT}{h^2}\right)^{3/2} \exp\left(-\frac{\text{IP}_2}{kT}\right) \tag{13}$$

Here, $n_{\text{vap}}$ represents the total vapor number density ($n_{\text{vap}} = \rho/m$), $x_e$, $x_{i1}$, $x_{i2}$ and $x_0$ stand for the fraction of electrons, singly charged ($Cu^+$) and doubly charged ($Cu^{2+}$) ions and neutral Cu atoms, respectively, which are defined as $x_e = n_e/n_{\text{vap}}$, etc. Further, $h$ is the Planck constant, and the other symbols have been explained above. Note that the difference between the electronic partition functions of the two ion stages was neglected in the above formulas.

The two Saha–Eggert equations are combined with two other equations, i.e. for the conservation of matter, and the conservation of charge, respectively:

$$x_0 + x_{i1} + x_{i2} = 1 \tag{14}$$

$$x_{i1} + 2x_{i2} = x_e \tag{15}$$

Finally, the vapor temperature ($T$) in the Saha–Eggert equations is adopted from the internal energy density (see Eq. (10) above).

These five equations (Eqs. (10), (12)–(15)) are solved together to calculate the five unknown values ($x_e$, $x_{i2}$, $xi_2$, $x_0$ and $T$), from which the number densities of electrons, $Cu^+$, $Cu^{2+}$ and $Cu^0$ can be obtained. The Newton–Raphson method [140] was applied to solve this strongly nonlinear system of equations. As discussed above, this system of equations can be extended with additional Saha–Eggert equations, when more multiply charged ions need to be considered. For every new unknown, an extra equation is added, so that the system remains solvable, and the new unknown value is also included in the other equations (conservation of matter and charge, and equation for internal energy density).

This system of equations is solved at every position in the plume, except in the first position near the target surface, where the main source of ions and electrons is given by thermionic emission from the heated surface [39]. This is described by the Langmuir–Saha equation [39,141–143]:

$$\frac{x_{i1}}{x_0} \approx \exp\left(\frac{\phi - \text{IP}_1}{kT_s}\right) \tag{16}$$

where $\phi$ is the electronic work function ([133]; see Table 1), and the other symbols are declared above. Assuming that only singly charged ($Cu^+$) ions are formed, and combining the Langmuir–Saha equation with the equations for conservation of matter ($x_0 + x_{i1} = 1$) and conservation of charge ($x_{i1} = x_e$), yields three equations for three unknowns. From the fractions ($x$), the number densities of electrons, $Cu^+$ and $Cu^0$ can be obtained, based on the total vapor density (see above).

### 2.4. Laser beam absorption in the plasma

Because of the formation of a plasma in front of the target, the laser beam will be partially absorbed before it reaches the target, i.e. so-called 'plasma shielding' [95]. Laser radiation is absorbed primarily by inverse Bremsstrahlung, which involves the absorption of a photon by a free electron. The electron is raised to a higher state in the continuum. This process must occur within the field of a heavy particle (ion or neutral), so that momentum is conserved [39]. Photo-ionization of excited states contributes only for energetic photons impinging on easily ionized gas mixtures [9], and is neglected here. The two contributions to inverse Bremsstrahlung are electron-neutral and electron-ion inverse Bremsstrah-

lung. Their absorption coefficients are given by [9]:

$$\alpha_{\mathrm{IB},e-n}=\left[1-\exp\left(-\frac{hc}{\lambda kT}\right)\right]Qn_e n_0 \qquad (17)$$

$$\alpha_{\mathrm{IB},e-i}=\left[1-\exp\left(-\frac{hc}{\lambda kT}\right)\right]\frac{4e^6\lambda^3 n_e}{3hc^4 m_e} \times\left(\frac{2\pi}{3m_e kT}\right)^{1/2}(Z_1^2 n_{i1}+Z_2^2 n_{i2}) \qquad (18)$$

Here, $\lambda$ is the laser wavelength, $Q$ is the cross section for photon absorption by an electron, during a collision with the neutrals (taken here as $10^{-36}$ cm$^5$) [9], and the other symbols have been explained above. The common factor in both formulas $(1-\exp(-hc/\lambda kT))$ accounts for stimulated emission [9].

### 2.5. Coupling of the different parts of the model

The different parts of the model are strongly coupled. On one hand, the laser–target interaction leads to evaporation, and the resulting vapor density, velocity and temperature are used as input for the plume expansion and plasma formation. On the other hand, the absorption of the laser beam in the plasma represents an important coupling back, both to the plume expansion (gain and loss terms in the equation for conservation of energy), and to the laser–solid interaction, because the laser energy can be considerably attenuated (plasma shielding) before it reaches the target, leading to less efficient target heating, melting and vaporization.

Hence, the different parts of the model need to be solved simultaneously as a function of time, in order to obtain an overall picture of the mechanism of laser ablation of a Cu target, with plume expansion and plasma formation.

## 3. Results of the model

The calculations are performed for a laser with wavelength of 266 nm, and a Gaussian-shaped laser pulse, illustrated in Fig. 1 (solid line). The pulse has a width (full-width at half-maximum, FWHM) of 10 ns, and the peak laser irradiance (or intensity) is $10^9$ W/cm$^2$. Integrated over the entire pulse, this yields a fluence of 10.6 J/cm$^2$. In our calculations, we follow only one laser pulse. The dashed line in Fig. 1 shows the laser intensity arriving at the target, after passing through the plume (plasma). It is clear that the laser intensity at the target drops significantly after approximately 10 ns, as a result of plasma shielding of the original laser pulse. After this significant drop, which results in a weaker plasma, and hence less plasma shielding, the laser intensity at the target rises again, but as time evolves further, the laser intensity at the target continues to decrease. This illustrates that a significant fraction of the original laser intensity is absorbed in the plasma, before it can reach the target. In other words, the laser intensity, which is really used for the ablation can be much lower than the initial laser intensity.

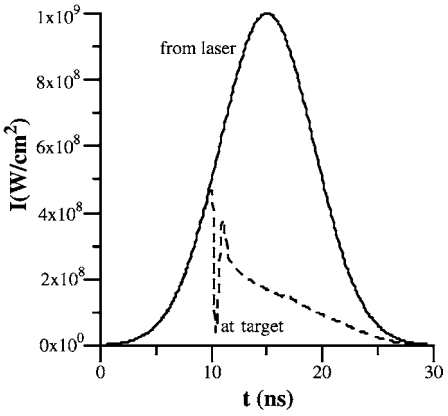


Fig. 1. Laser intensity-time profile assumed in the model. It is a Gaussian-shaped pulse with 10 ns full-width at half-maximum (FWHM), and maximum irradiance of $10^9$ W/cm$^2$. The dashed line represents the calculated laser intensity arriving at the target, after passing through the plume (plasma).

### 3.1. Target heating, melting and vaporization

Initially, the Cu target is at room temperature. However, as a result of the incoming laser beam, the target will be heated. The calculated temperature distribution in the target is depicted as a function of time during and after the laser pulse

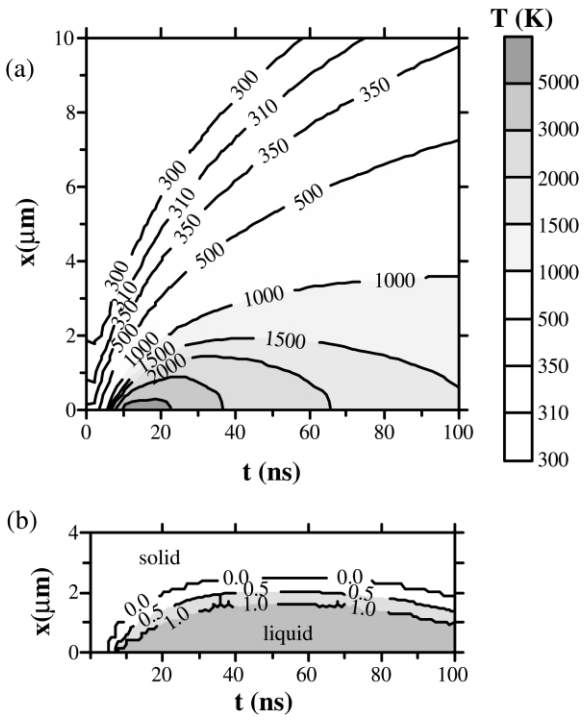


Fig. 2. Calculated temperature distribution in the target (a), and calculated solid/liquid regions in the target as a result of melting (b), as a function of time, for the conditions shown in Fig. 1. The original target surface is at 0 μm.

in Fig. 2a. The temperature is at maximum at the surface of the target, as expected. The maximum temperature of approximately 6750 K is reached between 10 and 20 ns, i.e. when the laser irradiance is at maximum. When time evolves, the region with elevated temperature (i.e. above room temperature) expands, due to thermal conduction (see Eq. (1)). For the conditions under study, the heating is more or less limited to the first 10 μm of the target. As far as melting is concerned, only a few micrometer is influenced, as appearing in Fig. 2b, which shows the solid and liquid (molten) phases in the target, as well as the transition region, which is partly molten (with temperature equal to melting point). Although the surface temperature drops significantly after the laser pulse, the first 2 μm of the target still remains in molten phase for quite a long time. Only after approximately 60 ns, resolidification of the melt starts to occur, and the melt depth starts to drop slowly.

The surface temperature and the melt depth are also plotted as a function of time in Fig. 3a, b respectively). Fig. 3a shows a little dip in the

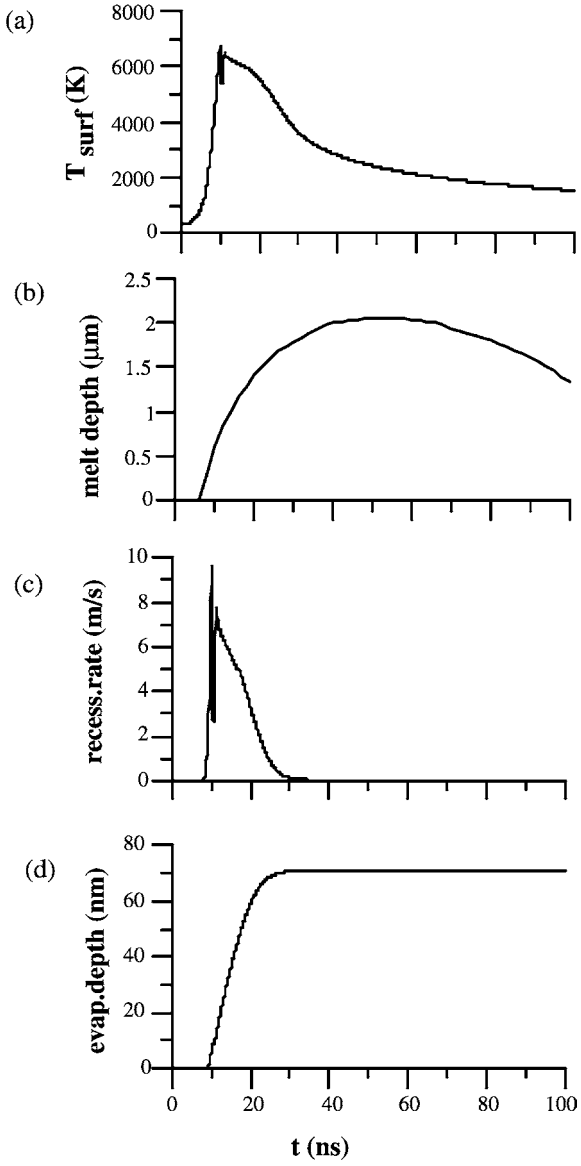


Fig. 3. Calculated temperature at the target surface (a), melt depth in the target (b), target surface recession rate due to evaporation (c) and depth of evaporation (d), as a function of time, for the conditions shown in Fig. 1.

surface temperature at approximately 10 ns, which corresponds to the dip in the laser intensity at the target (see Fig. 1). After 10–20 ns, the surface temperature begins to drop, but it is still approximately 2000 K at 100 ns, for the conditions under study. The target melting starts to occur at approximately 8 ns (see Fig. 3b), when the temperature begins to rise significantly. The melt depth increases to approximately 2 μm at 40–60 ns, i.e. clearly after pulse termination. After a longer time, it starts decreasing slowly, but it is still approximately 1.5 μm after 100 ns.

Fig. 3 also gives information on the target evaporation. The surface recession rate due to evaporation (Fig. 3c) is calculated from the flux of evaporated atoms, in the following way [34]:

$$R_{\text{recession}} = \frac{dx_{\text{evap}}}{dt} = \frac{j_{\text{evap}} M}{\rho} \tag{19}$$

$M$ and $\rho$ are the molecular mass of the atoms (kg) and the mass density (kg/m$^3$), respectively. The flux of evaporated atoms (m$^{-2}$ s$^{-1}$) is obtained from the vapor pressure at the surface temperature ($p(T_s)$; see Eq. (3) above):

$$j_{\text{evap}}(T_s) = \frac{A p(T_s)}{\sqrt{2\pi M R T_s}} \tag{20}$$

Here, $A$ represents a sticking coefficient, which is usually taken equal to one for metals. The other parameters have been defined before.

As shown in Fig. 3c, the calculated surface recession rate due to evaporation reaches a maximum of almost 10 m/s, and it shows a very similar profile as the laser intensity at the target (Fig. 1), including the dip at approximately 10 ns. This means that evaporation also ceases at pulse termination (ca. 30 ns). Indeed, from Clausius–Clapeyron equation it follows that evaporation dramatically slows down when the surface temperature drops below the boiling temperature.

From the surface recession rate due to evaporation, the depth of evaporation can be obtained, and the latter is plotted as a function of time in Fig. 3d. The evaporation depth rises as a function of time, starting from approximately 10 ns, and it reaches a constant value of ca. 70 nm, after approximately 25–30 ns, when the surface recession rate has dropped to zero. Comparing Fig. 3b,d tells us that the evaporation process affects only the surface layer, till a depth which is a factor of 30 smaller than the depth at which melting takes place.

In our model, material removal is solely attributed to vaporization. Hence, the thickness of the evaporated layer, or evaporation depth (ca. 70 nm), represents a lower limit of the crater depth, i.e. in case that vaporization is the only material removal mechanism. However, in laser ablation experiments, splashing of melt due to the plume recoil is observed (see Section 1.4 above). If we assume that the melt is completely ejected before resolidification occurs, the melt depth (ca. 2 μm) can be considered as an upper limit for the crater depth. In the book of Ready (Table 3.8, p. 111) [39], a measured crater depth of 2.2 μm was reported, for laser ablation by a 44 ns laser pulse with irradiance of $10^9$ W/cm$^2$, i.e. similar conditions as under study here. This would indeed suggest that splashing of molten material is responsible for a great deal of the material removal.

### 3.2. Plume expansion and plasma formation

Fig. 4 shows the calculated vapor density in the evaporated plume (a), the plume velocity (b) and vapor temperature (c), at different times, for the conditions mentioned above. It is worth mentioning that the initial conditions (i.e. before the laser pulse starts) assumed in our calculations, are a vapor density of $10^{18}$ m$^{-3}$ (which corresponds to a residual pressure of $10^{-7}$ atm), zero vapor velocity, a vapor temperature of 300 K, and a residual ionization degree in the plume of $10^{-10}$. These assumed initial conditions were not found to be critical for the calculation results.

It is clear from Fig. 4, for the different times shown in this figure, that the vapor density is highest at the target (i.e. almost $5\times10^{27}$ m$^{-3}$; not so clearly seen in the figure). It drops gradually as a function of distance in the plume, and very rapidly at the plume front. As time evolves, the plume becomes longer. For the laser ablation conditions under study, the plume length is calcu-

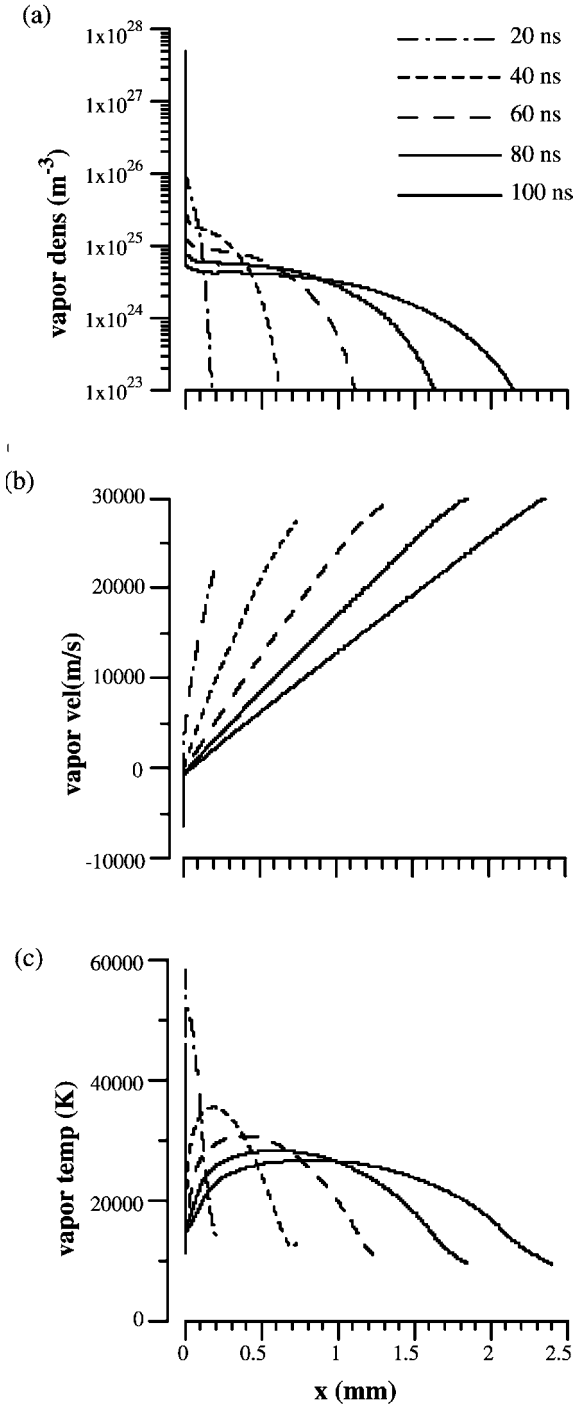


Fig. 4. Calculated density (a), velocity (b) and temperature (c) distributions in the vapor plume, at different times, for the conditions shown in Fig. 1.

lated in the order of 0.1 mm after 20 ns, and approximately 2 mm after 100 ns. Note that these values are calculated for plume expansion in vacuum. For expansion in a background gas at 1 atm, the vapor plume will be considerably shorter (see Section 1.3 above). The plume velocity (Fig. 4b) increases towards the end of the plume, and reaches maximum values of 20 000–30 000 m/s. Close to the target, the vapor velocity is calculated to be negative (ca. −4500 m/s at 20 nm, and approximately −6000 till −6300 m/s at 40 till 100 ns. This probably represents the plume recoil back to the target, which can give rise to target liquid splashing (see Section 1.4 above). The vapor temperature distribution in the plume is presented in Fig. 4c. It is calculated in the order of 10 000–50 000 K, and decreases slightly as a function of time. This temperature drop is most pronounced after 20 ns. Indeed, at 20 ns, the calculated temperature is much higher than at later times, because the laser pulse yields heating of the evaporated plume. At 40 ns, the laser pulse is already terminated, which explains the lower temperature. The further drop as time evolves represents cooling due to plume expansion. It should be noted that at the plume front a peak in the temperature was calculated, but this has no physical meaning, because the calculated vapor density at this position was very low, indicating that the plume was terminated.

Fig. 5 shows the plume characteristics in detail at 15 ns, i.e. at the maximum of the laser pulse. The vapor density in the plume (Fig. 5a) decreases away from the target. The plume length at this time is calculated at approximately 0.1 mm. The corresponding vapor temperature (Fig. 5b) is approximately 50 000 K at small distance (near the target), and it drops to approximately 15 000 K at the plume front. From this vapor temperature, the ionization degree, or the fraction of $Cu^0$ atoms, $Cu^+$ and $Cu^{2+}$ ions and electrons, is calculated with the Saha–Eggert equation (see above; Eqs. (12) and (13)). Fig. 5c illustrates that the $Cu^0$ atoms are only present near the target. The rest of the plume is more or less fully ionized at the laser conditions under study. In the first 0.03 mm from the target, where the vapor temperature is very high, the majority of Cu atoms is even doubly

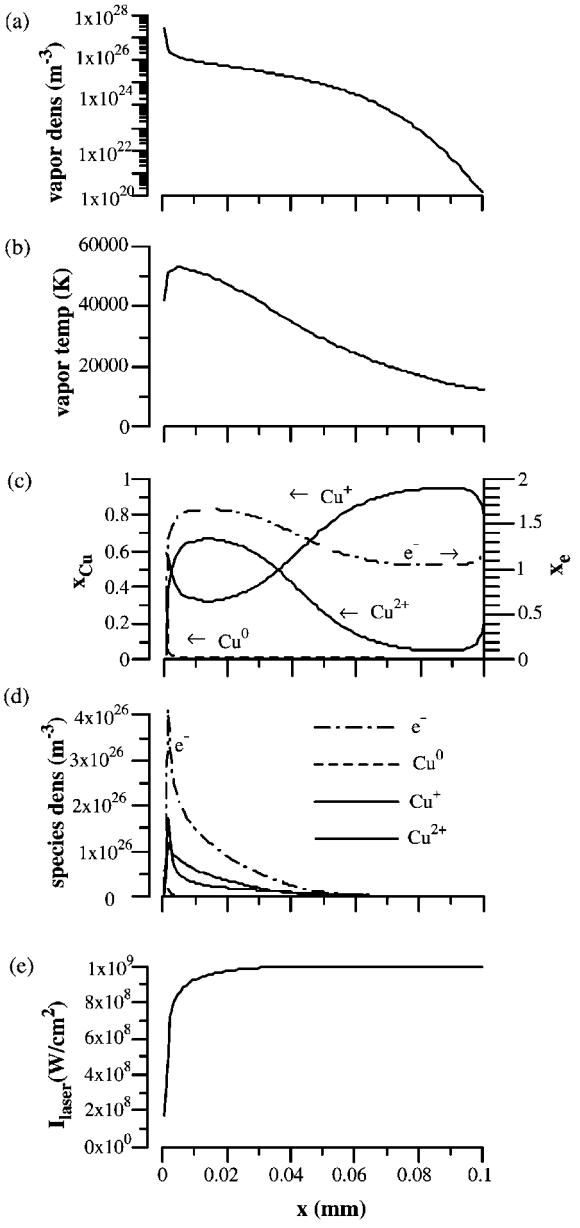


Fig. 5. Calculated density distribution (a), temperature distribution (b), fraction of $Cu^0$ atoms, $Cu^+$ and $Cu^{2+}$ ions and electrons (c), density distributions of these species (d) in the vapor plume, and laser intensity as a function of position in the plume (decreasing towards the target, as a result of plasma shielding) (e), at 15 ns, for the conditions shown in Fig. 1.

ionized ($Cu^{2+}$). At further distance, when the vapor temperature drops, the $Cu^+$ ions become dominant. The fraction of electrons is equal to the sum of $Cu^+$ ions and two times the $Cu^{2+}$ ions (see above, Eq. (15)). This explains why it is almost equal to two in the beginning of the plume, when the $Cu^{2+}$ ions are dominant (see dash-dotted line and right axis in Fig. 5c). From the fraction of the species, multiplied with the vapor density, the species densities in the plume are obtained, and the results are plotted as a function of distance in the plume in Fig. 5d. The $Cu^0$ atom density is very high near the target (order of $5\times10^{27}$ $m^{-3}$; note that the *y*-axis in Fig. 5d is truncated at $4\times10^{26}$ $m^{-3}$, in order not to hide all other density values), but it drops significantly in the first few micrometers from the target. The densities of the charged species (electrons and ions) reach a maximum at approximately 1 μm from the target, i.e. where the vapor density is still very high (see Fig. 5a) and the plasma is almost fully ionized. The $Cu^+$ and $Cu^{2+}$ ion densities are very comparable here. After this maximum, the densities drop very quickly, which is most pronounced for the $Cu^+$ ions, and which is due to the steep decrease in vapor density (see Fig. 5a). From these densities, the absorption of the incoming laser beam in the plasma is calculated, i.e. plasma shielding, due to inverse Bremsstrahlung (IB). It appears that electron-ion IB (Eq. (18) above) is negligible in the entire plasma. Indeed, the electron and ion densities are too low (in spite of the fully ionized plasma, but the plume density is too low), to compensate for the very small constant factor in Eq. (18). Electron-neutral IB (Eq. (17) above), however, is important in the first 10 μm near the target, where both electron and $Cu^0$ atom densities are still sufficiently high. This absorption process yields a drop in the laser intensity in the first 10 μm adjacent to the target, as is clear from Fig. 5e. The calculated laser intensity arriving at the target is approximately $1.7\times10^8$ $W/cm^2$, which corresponds to the value shown in Fig. 1.

Fig. 6 shows details of the plume at 100 ns. It is clear that the plume has become much longer now (note the different scale of the *x*-axis!), as was also illustrated in Fig. 4a. However, the shape of the plume density is very similar (see Fig. 6a),

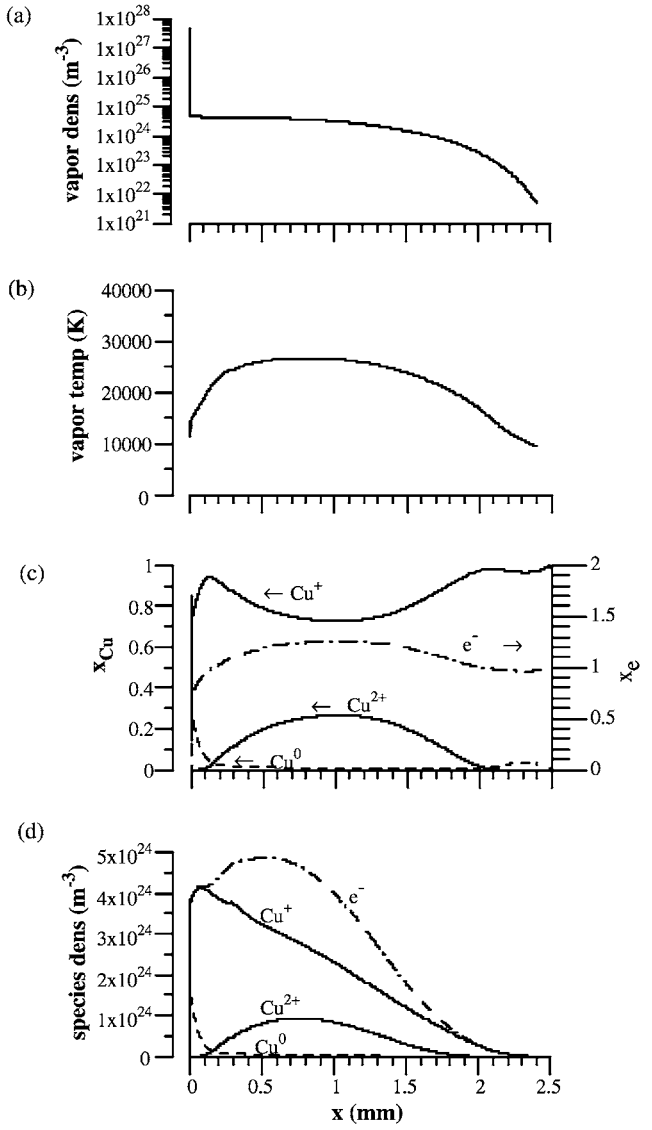


Fig. 6. Calculated density distribution (a), temperature distribution (b), fraction of $Cu^0$ atoms, $Cu^+$ and $Cu^{2+}$ ions and electrons (c), and density distributions of these species (d) in the vapor plume, at 100 ns, for the conditions shown in Fig. 1.

with a maximum near the target (of almost $5\times10^{27}$ $m^{-3}$), a slight decrease as a function of distance, and a steep drop at the plume front. The vapor temperature (at maximum 25 000 K; see Fig. 6b) is somewhat lower than at 15 ns, as was explained above (i.e. no more heating by the laser, and cooling due to plume expansion). Consequently, the plasma is somewhat less ionized. More specifically, the $Cu^{2+}$ ions are of less importance than the $Cu^+$ ions in the entire plume. The $Cu^0$ atoms are still only present near the target, as appears from Fig. 6c, d. Indeed, the $Cu^0$ atom density near the target is almost $3\times10^{27}$ $m^{-3}$ (the *y*-axis of Fig. 6d is now truncated at $5\times10^{24}$ $m^{-3}$, so that the other density values remain visible), but it drops very rapidly as a function of distance from the target. The $Cu^+$ ion density, however, decreases very slowly towards the plume front, and the $Cu^{2+}$ ion and electron density reach their maximum between 0.5 and 1 mm from the target. Plasma shielding of the laser beam by IB does not play a role anymore at 100 ns, since the laser pulse is already terminated at 30 ns (see above).

## 4. Effect of target surface reflectivity

The target surface reflectivity to be used in the model (see above, Eq. (2)) is not known very accurately. It is in general close to 1 for metals, but it can drop to values as low as 0.1 during laser ablation (see Section 2.1). We have used an intermediate value of 0.34 (see above). However, the choice of this parameter will affect the calculation results, because it determines the amount of laser energy that can be absorbed in the target, and that gives rise to target heating, melting and vaporization, and hence to the plume and plasma formation. Therefore, we have investigated the effect of this parameter on the calculation results, as is presented in Fig. 7. When the target surface reflectivity, $\Re$, increases, less energy can go into the target, leading to a lower temperature in the target (Fig. 7a), less melting (Fig. 7b) and evaporation (Fig. 7c,d), and consequently a lower vapor density (Fig. 7e), a shorter plume (Fig. 7f), a lower plume velocity and temperature (Fig. 7g), and a less ionized plasma (Fig. 7h). The effect is limited for low values of $\Re$, but it becomes significant for values approaching 1. Indeed, when $\Re$ is equal to 1, no energy can enter the target, and there will be no heating, melting, vaporization, plume and plasma formation. When $\Re$ is equal to

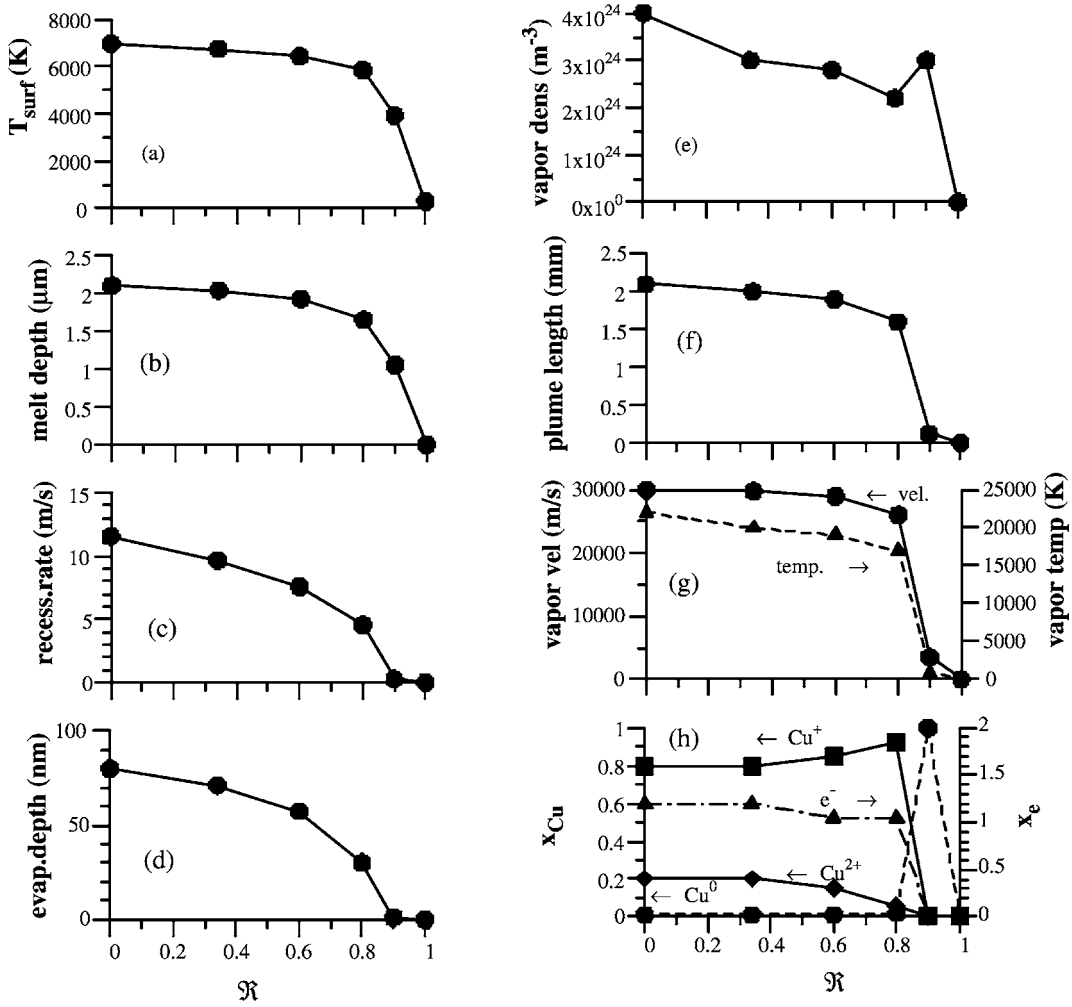


Fig. 7. Calculated target surface temperature (a), melt depth (b), surface recession rate due to evaporation (c), evaporation depth (d), average vapor density in the plume (e), plume length (f), vapor velocity and average temperature in the plume (g), and typical fraction of $Cu^0$ atoms, $Cu^+$ and $Cu^{2+}$ ions and electrons in the plume (h), assuming different values of the target reflectivity, ℜ.

0.9, 10% of the laser energy can enter the target, and this can result already in a significant heating (to a temperature of almost 4000 K, see Fig. 7a) and melting (to a depth of more than 1 μm, see Fig. 7b). However, the evaporation is still of minor importance (Fig. 7c,d), so that only a short vapor plume is formed (Fig. 7f), at low temperature and traveling with low velocity (Fig. 7g). Also, the plume is composed only of neutral Cu atoms, i.e. no plasma is formed yet (Fig. 7h). When ℜ is equal to 0.8, 20% of the laser energy can be used for target heating, yielding a higher temperature, more melting, as well as evaporation. Consequently, a longer plume will be formed, and the plume velocity and temperature will be higher, leading to almost fully ionized plasma. The vapor density was calculated to be a bit lower than for ℜ equal to 0.9 (see Fig. 7e), which is attributed to the faster expansion of the plume. When ℜ is further decreased, the target temperature, melting and vaporization still increase, and the vapor plume becomes longer, with higher density, velocity and

temperature, and the electron density in the plasma increases. However, the effect becomes less pronounced when $\Re$ approaches 0. Indeed, the difference between 100 and 90% laser energy entering the target (i.e. $\Re$ equal to 0 or 0.1) is much less than the difference between 10% and 0% (i.e. $\Re$ equal to 0.9 or 1). Since $\Re$ is expected to be rather small during laser ablation (see Section 2.1), our choice of $\Re$ equal to 0.34 [95] is probably a good choice, and the calculation results can be considered reliable.

## 5. Effect of laser intensity

We have also performed some calculations at different laser intensities, in the range $10^7$–$10^{10}$ W/cm$^2$. The same Gaussian-shaped laser pulses were assumed in all cases; only the intensities vary, as is presented in Fig. 8. The solid lines in this figure represent the original laser intensities, whereas the dashed lines denote the laser intensities arriving at the target, after plasma absorption. It appears from this figure that plasma shielding only takes place for laser intensities above $2\times10^8$ W/cm$^2$. Further, the plasma shielding becomes more pronounced at higher laser intensities. Consequently, the laser intensity arriving at the target was calculated to be rather similar, in spite of varying original laser intensities, as can be deduced from Fig. 8.

Fig. 9 illustrates some calculated quantities for different incoming laser intensities (or irradiances). As is clear from Fig. 9a, the laser fluence increases linearly with laser irradiance, which is logical, because the pulse shapes are kept the same. Further, at rising laser irradiance, the target heating (Fig. 9b), melting (Fig. 9c) and vaporization (Fig. 9d,e) increase, the plume becomes somewhat more dense (Fig. 9f), longer (Fig. 9g) and hotter (Fig. 9i), it travels with higher velocity (Fig. 9h), and it becomes more ionized (Fig. 9j). At a laser irradiance of $10^7$ W/cm$^2$, the heating is very moderate, yielding a surface temperature of less than 500 K. Consequently, neither melting nor vaporization take place, and no plume is formed. At $10^8$ W/cm$^2$ laser intensity, the heating becomes more important, and melting occurs. However, the vaporization is still very limited, leading to a very short and rather cool vapor plume (temperature approx. 800 K), consisting only of neutral $Cu^0$ atoms (hence, no ionization takes place). For a laser intensity of $2\times10^8$ W/cm$^2$, the target heating and melting are still more significant, and vaporization starts playing a more important role. However, the vapor plume is still rather short and cool (approx. 900 K), and plasma is not yet created. Upon further increasing the laser irradiance, target heating, melting and vaporization grow in importance, and the plume becomes longer and much hotter, leading to plasma formation. At $5\times10^8$ W/cm$^2$, the plume is already almost fully ionized into $Cu^+$ ions (approx. 85%). For higher laser irradiance, the fraction of $Cu^{2+}$ ions rises, and exceeds the $Cu^+$ fraction at $5\times10^9$ W/cm$^2$, because of still higher plume temperature. Consequently, also the electron density in the plume increases with laser irradiance, so that more plasma shielding can occur, as was indeed illustrated in Fig. 8.

## 6. Comparison with other calculated or experimental results

Comparison with other data from the literature, obtained either by models or experiments, is not straightforward, because the laser ablation conditions in the literature (e.g. laser wavelength, pulse duration, irradiance, target material, expansion in vacuum or in a background gas) are not always clearly described, or they are not exactly the same, and the results will be different for different conditions. However, we have attempted to make at least some qualitative comparisons, to check our modeling results.

### *6.1. Comparison with other calculation results*

In spite of the multitude of papers in the literature describing models for laser–solid interaction, plume expansion and plasma formation (see Section 1.2 above), not many of these papers show detailed calculation results for conditions comparable to the ones under study here. However, a few papers gave results that can be compared with our data. Amoruso [36] calculated the plume temperature, neutral atom and electron density for a 6 ns laser pulse at 350 nm on an Al target. For

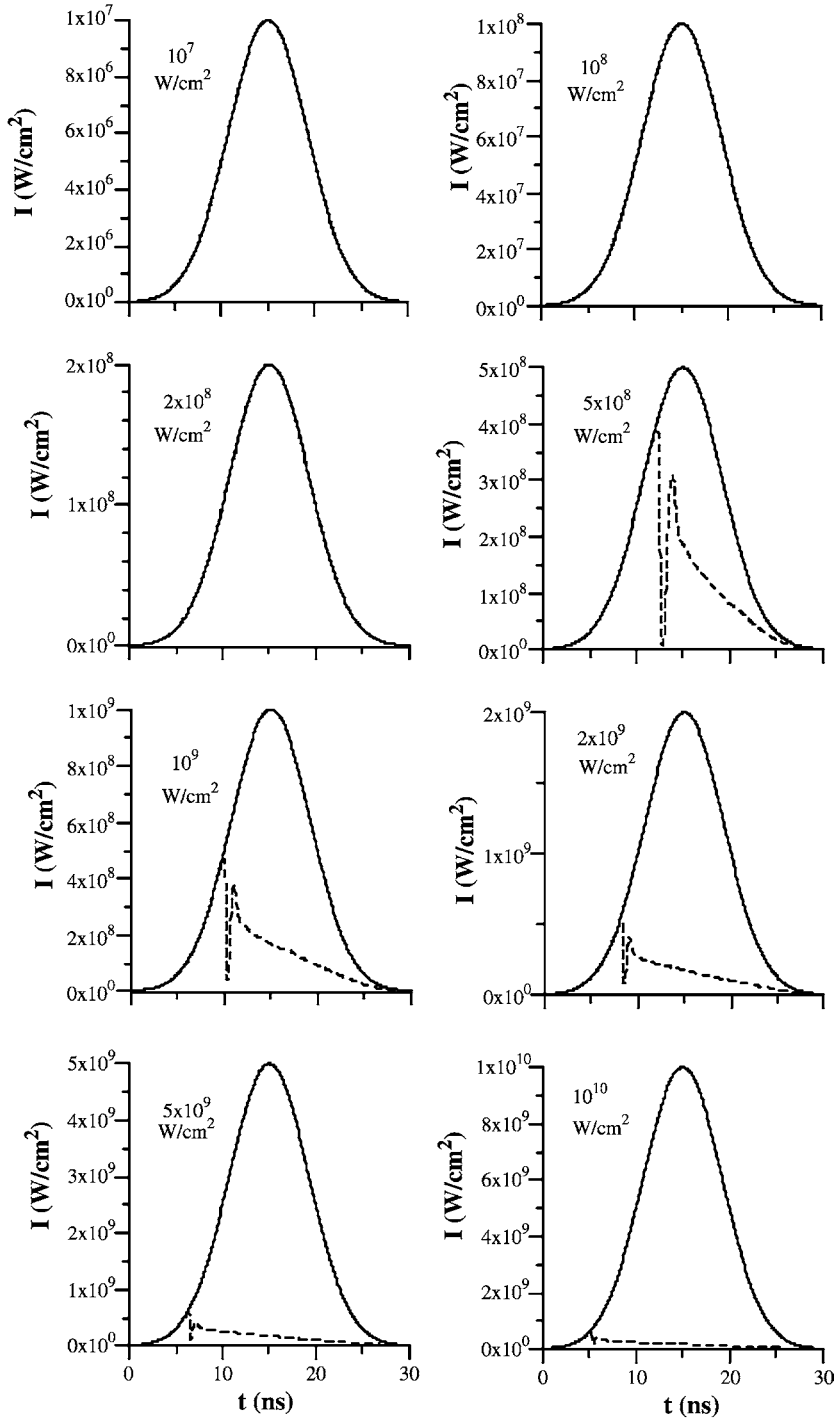


Fig. 8. Laser intensity-time profiles for different values of laser irradiance, assuming the same pulse shape of 10 ns (FWHM). The dashed lines represent the calculated laser intensities arriving at the target, after passing through the plasma.

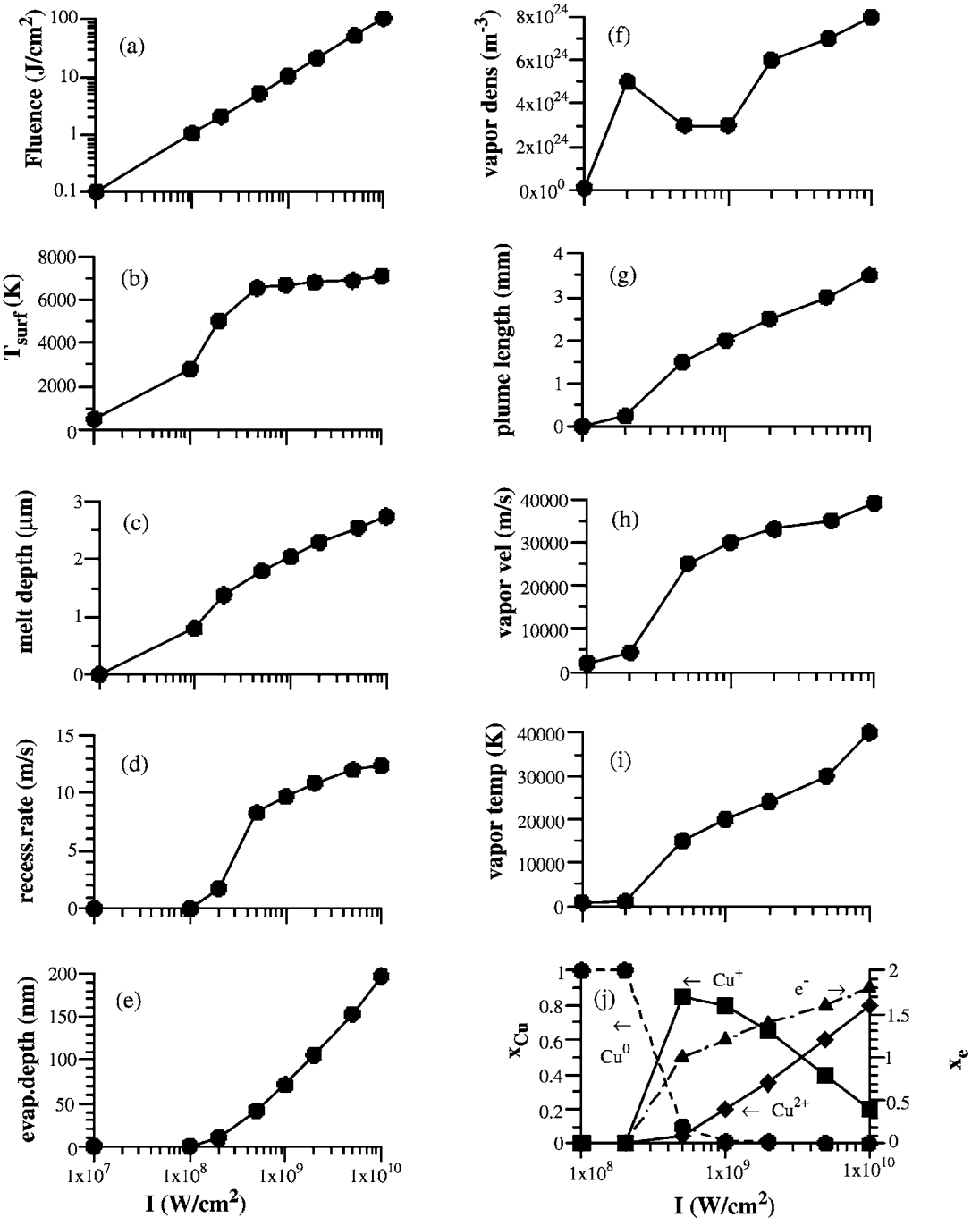


Fig. 9. Laser fluence corresponding to different values of laser irradiance (a), as well as calculated target surface temperature (b), melt depth (c), surface recession rate due to evaporation (d), evaporation depth (e), average vapor density in the plume (f), plume length (g), plume velocity (h), average temperature in the plume (i), and typical fraction of $Cu^0$ atoms, $Cu^+$ and $Cu^{2+}$ ions and electrons in the plume (j), as a function of laser irradiance.

an irradiance of $10^9$ W/cm$^2$, the electron density was in the order of $10^{26}$ m$^{-3}$, which was found to be higher than the neutral density. The plume temperature was in the order of 20 000 K. Both electron density and plume temperature increased drastically with rising laser intensity up to a value of $1.5\times10^9$ W/cm$^2$. For higher laser intensities, the rise was not so pronounced. These results are in satisfactory agreement with our data. Kar and Mazumder [38] calculated results for a 30 ns laser pulse of 248 nm on a Nb target, at a laser irradiance of $5\times10^8$ W/cm$^2$. The melt depth was reported to be 1–2 μm. The dimensions of the plume were in the order of 0.1–1 mm, increasing with time. The plume temperature was approximately 10 000 K, resulting in an ion fraction of several%. This is lower than our results, but the melt depth and plume dimension are in good agreement. Finally, Zhang et al. [37] performed calculations for a 10 ns laser pulse at 248 nm on a graphite sample, for a laser irradiance of $3\times10^8$ W/cm$^2$. Results are reported after 2, 5 and 10 ns. At 10 ns, the plume length was approximately 0.1–0.2 mm. The plume velocity was in the order of $10^4$ m/s, and the plume temperature was approximately 10 000–20 000 K. At the end of the plume, a pronounced maximum of approximately 100 000 K was shown, similar to our observations. However, as discussed above (Section 3.2), this temperature peak corresponds to a region where the plume density has dropped to very low values, so it has no real physical meaning. In general, these calculation results were in good agreement with our data.

### 6.2. Comparison with experimental data

Beside these modeling studies, several papers report measurements in the laser-ablated plume, mainly for the plume temperature and electron density. Sometimes these experiments were carried out in a background gas. However, preliminary calculations from our group show that the plume temperature and hence the electron density are not too much different for expansion in vacuum or in 1 atm background gas [128]. The major difference is expected in the rate of change of physical properties, which will be much faster in vacuum, because of the faster expansion. Russo and coworkers [144] studied a 3 ns laser pulse at 266 nm on a Si target, for laser irradiance in the range of $2\times10^9$–$8\times10^{10}$ W/cm$^2$. At $2\times10^9$ W/cm$^2$, the plume temperature was approximately 15.000 K, and the electron density was ca. $5\times10^{24}$ cm$^{-3}$, at a distance of 1.8 mm and a delay time of 30 ns. Doyle et al. [145] also reported electron density values in the order of $1–10\times10^{24}$ cm$^{-3}$, decreasing with distance from the target. The laser ablation conditions in this case were a pulse of 30 ns (FWHM), at 248 nm, on a Mg target, for an irradiance of $1.25–3\times10^8$ W/cm$^2$. Hence, the electron density was in the same order of magnitude, but for lower irradiance, which is probably attributed to a difference in laser conditions (laser pulse, wavelength), or target. However, in general the agreement is reasonable. Moreover, the plume length appeared to be in the order of 0.5 mm, at 30 ns, and it increases with time, which is in correspondence with our results. An electron density in the order of $10^{24}$ m$^{-3}$ was also measured in Ref. [146] for a laser irradiance of $10^{10}$ W/cm$^2$, a pulse of 7 ns, at 355 nm, and an Al target. Monge et al. [147] measured a plume temperature of approximately 10 000 K at maximum, and an electron density approximately $10^{22}$–$10^{23}$ m$^{-3}$. This is lower than our calculated results, but the delay time of measurement was several microseconds, which is much longer than in our study, and it is illustrated, both in our calculation results, as well as in Ref. [147] that the plume temperature and hence the electron density drop as time evolves, as a result of plume expansion. Hafez et al. [148] also measured electron densities in the order of $10^{22}$ m$^{-3}$, for a laser pulse of 7 ns, at 335 nm, an irradiance of $10^{10}$ W/cm$^2$, and a Cu target, both for expansion in vacuum and in 5 Torr argon. These reported electron density values are also lower than our calculation results, but they were probably also measured at a later time (not reported in the paper), because the plume length was in the order of 14 mm. Finally, in Ref. [149] it was reported that for pulsed ns UV lasers on metal targets, a dense and highly ionized plasma is created at a laser irradiance in the order of $4\times10^8$ W/cm$^2$. The measured electron density at approximately 50–100 ns was in the order of

$10^{24}$ $m^{-3}$ for a laser irradiance of $5\times10^{8}$ $W/cm^2$, and it dropped over several orders of magnitude as a function of time (i.e. two orders of magnitude at 1 μs).

Beside electron density measurements, the ions have also been investigated in laser ablation experiments. Dreyfus [150] has reported laser-induced fluorescence measurements of $Cu^0$, $Cu^+$ and $Cu_2$, as a function of fluence, to elucidate the mechanisms playing a role in laser ablation. Amoruso et al. [151,152] measured energy distributions of ions in ns laser produced plasmas of Al and Cu targets at visible and UV wavelengths, for a laser fluence in the range of 3–60 $J/cm^2$, to study the importance of various plasma processes (i.e. inverse Bremsstrahlung absorption, photo-ionization, electron impact ionization and excitation). Franghiadakis [153] also measured ion kinetic energy distributions in the laser-ablated plume, for UV ns-pulsed lasers on various materials, including Cu. It was shown that not only $Cu^+$ ions, but also $Cu^{2+}$ ions were present. The $Cu^+$ intensity was typically a factor of 5–10 times higher than the $Cu^{2+}$ signal, but the laser fluence was somewhat lower than in our case (i.e. 1–8 $J/cm^2$). The facts that multiply charged ions were detected, not only in Ref. [153], but also in several other papers referred to in Ref. [153], are at least a qualitative validation of our calculations. From the measured energy distributions, an effective plasma temperature in the range of 20.000–100.000 K was deduced, which also correlates well with our data.

Finally, the phenomenon of plasma shielding is also studied in a number of papers. Russo and coworkers [105,154] found that the mass removal rate depends strongly on the laser irradiance, but a roll-off in this dependence was observed between $1\times10^{8}$ and $5\times10^{8}$ $W/cm^2$ (depending on the material), which is attributed to the onset of plasma shielding. Indeed, it is generally stated (e.g. [22]) that for ns-pulsed lasers, with laser irradiance below $2.5\times10^{8}$ $W/cm^2$, only vaporization takes place, and a plasma is only created for a laser irradiance above $2.5\times10^{8}$ $W/cm^2$. The plasma becomes fully ionized at approximately $5\times10^{8}$ $W/cm^2$, and it becomes opaque for the incoming laser energy at approximately $10^{9}$ $W/cm^2$. This correlates with our calculations for the onset of plasma formation and plasma shielding.

## 7. Conclusion

We have presented a model for ns-pulsed laser ablation of a Cu target that describes:

1. Laser–solid interaction, yielding heating, melting, and vaporization of the target material;
2. expansion of the evaporated material plume in vacuum;
3. plasma formation, generating electrons, $Cu^+$ and $Cu^{2+}$ ions, beside the Cu atoms;
4. plasma shielding of the incoming laser light.

The results include the temperature distribution inside the target, the melt depth, the amount of evaporation, the vapor density, velocity and temperature distribution in the plume, as well as the resulting ionization degree, and the density profiles of electrons, $Cu^0$ atoms, $Cu^+$ and $Cu^{2+}$ ions in the plasma. All these results are presented as a function of time during and after the laser pulse.

For a typical laser irradiance of $10^{9}$ $W/cm^2$ (i.e. fluence of approx. 10 $J/cm^2$ for the pulse under study), it is found that the temperature in the target rises till a few 1000 K, and is at its maximum near the surface. The melt depth is calculated to be in the order of 2 μm. The evaporation depth, however, is estimated to be only approximately 70 nm, for one laser pulse. The vapor plume expands as time evolves: the plume length is in the order of 0.1 mm after 20 ns, and it increases to ca. 2 mm after 100 ns. The vapor density in the plume is very high near the target (approx. $5\times10^{27}$ $m^{-3}$), but it decreases rapidly to typical values of $10^{24}$–$10^{25}$ $m^{-3}$ in most of the plume. Moreover, the vapor density also decreases slightly upon plume expansion. The vapor velocity in the plume increases towards the end of the plume, where it is in the order of 30 000 m/s. The vapor temperature in the plume is calculated between 10 000 K and 40 000 K. At this high vapor temperature, the plume is more or less fully ionized, and in some regions of the plume, i.e. where the vapor temperature reaches its maximum, the $Cu^{2+}$ ions can even become dominant. Since the vapor plume is converted into plasma, part of the incoming laser

beam will be absorbed before reaching the target. For the laser ablation conditions under study, it was found that electron-neutral inverse Bremsstrahlung is mainly responsible for the plasma shielding.

Because the target surface reflectivity is subject to uncertainties (i.e. it is typically close to 1 for polished metals, but it can drop to values as low as 0.1 during laser ablation), we have explicitly investigated the effect of this parameter on the calculation results. When $\Re$ was increased from 0 to 1, the target heating, melting and vaporization were found to decrease, as well as the plume length, the vapor density, velocity and temperature in the plume, and the ionization degree and charged species densities in the plasma. This is logical, because when $\Re$ increases, the laser energy that can enter the target and give rise to target heating, melting and vaporization drops. The effect of $\Re$ is found to be much more pronounced at $\Re$ close to 1, and is only small for $\Re$ between 0 and 0.8. Since this parameter is probably rather small during laser ablation, our choice of 0.34 is probably a good choice.

Finally, we have also performed calculations for different laser intensities (or irradiance), in the range $10^7$–$10^{10}$ W/cm$^2$. A higher laser irradiance gives rise to more target heating, melting and vaporization, resulting also in a longer plume, a higher vapor density, velocity and temperature in the plume, and more charged species (i.e. higher ionization degree of the plasma), as is expected. For a laser irradiance of $10^7$ W/cm$^2$, the target heating is calculated to be very moderate, and neither melting nor vaporization takes place. When the laser irradiance increases to $10^8$ W/cm$^2$ or $2\times10^8$ W/cm$^2$, target heating and melting become more pronounced, but the evaporation is still limited, so that the vapor plume is still rather short and cool, and no plasma is formed. At higher laser irradiance ($5\times10^8$ W/cm$^2$), target evaporation becomes much more significant, the plume becomes longer and hotter, and a plasma is created. This results also in plasma shielding of the incoming laser light. For laser irradiance between $5\times10^8$ and $10^{10}$ W/cm$^2$, the target heating, melting and vaporization still increase, the plume becomes longer, and the vapor density, velocity and temperature, as well as the plasma ionization degree still rise. However, the difference is not so pronounced anymore, because a higher original laser irradiance yields more plasma shielding, so that the laser irradiance that actually reaches the target does not rise to a large extent.

The present model does not yet describe the expansion of the evaporated material into a background gas, and it does not consider the formation of particles. Hence, it is not directly suitable for the description of laser ablation as sample introduction method for the ICP, where the laser ablation cell is typically filled with gas at 1 atm, and where the particles are the main constituents of the flow transported to the ICP. In the next step, the present model will be used as a starting point for a more realistic description of laser ablation for the ICP, including the expansion in 1 atm background gas, and the formation of particles.

However, the goal of the present paper was to demonstrate that this basic model could already give insight in the various aspects playing a role in the laser ablation mechanism. From the satisfactory correlation between our calculation results and several other papers in the literature, reporting either modeling or experimental studies, even for expansion in a background gas, it can be concluded that our model presents already a realistic picture of the mechanisms playing a role in laser ablation.

## Acknowledgments

A. Bogaerts is indebted to the Flemish Fund for Scientific Research (FWO) for financial support. Z. Chen is financed by the IUAP-V project. A. Vertes acknowledges the support of the US Department of Energy under grant # DE-FG02-01ER15129.The authors also thank D. Günther, S. Mao, J.-M. Mermet and B. Garrison for the interesting discussions and A. Okhrimovskyy for the translation of the Russian papers.

## References

[1] M. Von Allmen, Laser Beam Interactions with Materials, Springer, Heidelberg, 1987.
[2] D.B. Chrisey, G.K. Hubler (Eds.), Pulsed Laser Deposition of Thin Films, Wiley, New York, 1994.

[3] S. Vijayalakshmi, M.A. George, J. Sturmann, H. Grebel, Pulsed laser deposition of Si nanoclusters, Appl. Surf. Sci. 127–129 (1998) 378–382.
[4] M.F. Becker, J.R. Brock, H. Cai, D.E. Henneke, J.W. Keto, J. Lee, W.T. Nichols, H.D. Glicksman, Metal nanoparticles generated by laser ablation, Nanostructured Mater. 10 (1998) 853–863.
[5] S. Ameer-Beg, W. Perrie, S. Rathbone, J. Wright, W. Weaver, H. Champoux, Femtosecond laser microstructuring of materials, Appl. Surf. Sci. 127–129 (1998) 875–880.
[6] A. Marcinkevicius, S. Juodkazis, M. Watanabe, M. Miwa, S. Matsuo, H. Misawa, J. Nishii, Femtosecond laser-assisted three-dimensional microfabrication in silica, Opt. Lett. 26 (2001) 277–279.
[7] F.H. Loesel, J.P. Fischer, M.H. Götz, C. Horvath, T. Juhash, F. Foack, N. Suhm, F.J. Bille, Non-thermal ablation of neural tissue with femtosecond laser pulses, Appl. Phys. B 66 (1998) 121–128.
[8] A. Vertes, R. Gijbels, F. Adams (Eds.), Laser Ionization Mass Analysis, Wiley, New York, 1993.
[9] L.J. Rakziemski, D.A. Cremers (Eds.), Laser-induced Plasmas and Applications, Marcel Dekker Inc, New York, 1989.
[10] J.D. Winefordner, I.B. Gornushkin, D. Pappas, O.I. Matveev, B.W. Smith, Novel uses of lasers in atomic spectroscopy, J. Anal. At. Spectrom. 15 (2000) 1161–1189.
[11] M.C. Galicia, A. Vertes, J.H. Callahan, Atmospheric pressure matrix-assisted laser desorption/ionization in transmission geometry, Anal. Chem. 74 (2002) 1891–1895.
[12] L. Van Vaeck, K. Poels, S. De Nollin, A. Hachimi, R. Gijbels, Laser microprobe mass spectrometry: principle and applications in biology and medicine, Cell Biol. Int. 21 (1997) 634–648.
[13] L.J. Radziemski, From LASER to LIBS, the path of technology development, Spectrochim. Acta Part B 57 (2002) 1109–1113.
[14] A. Montaser, M.G. Minnich, J.A. McLean, H. Liu, J.A. Caruso, C.W. McLeod, Sample introduction in ICP-MS, in: A. Montaser (Ed.), Inductively Coupled Plasma Mass Spectrometry, Wiley, New York, 1998, Chapter 3.
[15] R.E. Russo, Laser ablation, Appl. Spectrosc. 49 (1995) 14A–28A.
[16] D. Günther, S.E. Jackson, H.P. Longerich, Laser ablation and arc/spark solid sample introduction into inductively coupled plasma mass spectrometers, Spectrochim. Acta Part B 54 (1999) 381–409.
[17] D. Günther, I. Horn, B. Hattendorf, Recent trends and developments in laser ablation ICP mass spectrometry, Fresenius J. Anal. Chem. 368 (2000) 4–14.
[18] R.E. Russo, X. Mao, S.S. Mao, The physics of laser ablation in microchemical analysis, Anal. Chem. 74 (2002) 70A–77A.
[19] J.S. Becker, Applications of inductively coupled plasma mass spectrometry and laser ablation inductively coupled plasma mass spectrometry in materials science, Spectrochim. Acta Part B 57 (2002) 1805–1820.
[20] D. Günther, B. Hattendorf, C. Latkoczy, Laser ablation inductively coupled plasma mass spectrometry—It's the aerosol size that really matters, Anal. Chem. A-pages (submitted).
[21] S.H. Jeong, R. Greif, R.E. Russo, Numerical modeling of pulsed laser evaporation of aluminum targets, Appl. Surf. Sci. 127–129 (1998) 177–183.
[22] W. Svendsen, O. Ellegaard, J. Schou, Laser ablation deposition measurements from silver and nickel, Appl. Phys. A 63 (1996) 247–255.
[23] J.H. Yoo, S.H. Jeong, R. Greif, R.E. Russo, Explosive change in crater properties during high power nanosecond laser ablation of silicon, J. Appl. Phys. 88 (2000) 1638–1649.
[24] D. Bhattacharya, R.K. Singh, P.H. Holloway, Laser–target interactions during pulsed laser deposition of superconducting thin films, J. Appl. Phys. 70 (1991) 5433–5439.
[25] K. Watanabe, T. Iguchi, Modeling of vaporization processes of resonant laser ablation, Appl. Phys. A 69 (1999) S845–S848.
[26] A. Peterlongo, A. Miotello, R. Kelly, Laser-pulse sputtering of aluminum: vaporization, boiling, superheating, and gas-dynamic effects, Phys. Rev. E 50 (1994) 4716–4727.
[27] M. Aden, E. Beyer, G. Herziger, H. Kunze, Laser-induced vaporization of a metal surface, J. Phys. D: Appl. Phys. 25 (1992) 57–65.
[28] J.R. Ho, C.P. Grigoropoulos, J.A.C. Humphrey, Computational study of heat transfer and gas dynamics in the pulsed laser evaporation of metals, J. Appl. Phys. 78 (1995) 4696–4709.
[29] A. Vertes, Energy coupling and dissipation mechanisms in laser–solid interaction, in: J.C. Miller, D.B. Geohegan (Eds.), Laser Ablation: Mechanisms and Applications–II, AIP Conference Proceedings 288, AIP Press, New York, 1994.
[30] C.L. Liu, J.N. Leboeuf, R.F. Wood, D.B. Geobegan, J.M. Donato, K.R. Chen, A.A. Puretzky, Computational modeling of physical processes during laser ablation, Mater. Sci. Eng. B47 (1997) 70–77.
[31] K.R. Chen, J.N. Leboeuf, R.F. Wood, D.B. Geohegan, J.M. Donato, C.L. Liu, A.A. Puretzky, Laser–solid interaction and dynamics of laser-ablated materials, Appl. Surf. Sci. 96–98 (1996) 45–49.
[32] J.N. Leboeuf, K.R. Chen, J.M. Donato, D.B. Geohegan, C.L. Liu, A.A. Puretzky, R.F. Wood, Modeling of dynamical processes in laser ablation, Appl. Surf. Sci. 96–98 (1996) 14–23.
[33] A. Vertes, R.W. Dreyfus, D.E. Platt, Modeling the thermal-to-plasma transitions for Cu photoablation, IBM J. Res. Develop. 38 (1994) 3–10.
[34] L. Balazs, R. Gijbels, A. Vertes, Expansion of laser-generated plumes near the plasma ignition threshold, Anal. Chem. 63 (1991) 314–320.

[35] R.K. Singh, J. Narayan, Pulsed-laser evaporation technique for deposition of thin films: physics and theoretical model, Phys. Rev. B 41 (1990) 8843–8858.
[36] S. Amoruso, Modeling of UV pulsed-laser ablation of metallic targets, Appl. Phys. A 69 (1999) 323–332.
[37] Z. Zhang, Z-X. Han, G.S. Dulikravich, Numerical simulation of laser-induced plasma during pulsed laser deposition, J. Appl. Phys. 90 (2001) 5889–5897.
[38] A. Kar, J. Mazumder, Mathematical model for laser ablation to generate nanoscale and submicrometer-size particles, Phys. Rev. E 49 (1994) 410–419.
[39] J.F. Ready, Effects of High Power Laser Radiation, Academic Press, New York, 1971.
[40] S.S. Mao, X.-L. Mao, R. Greif, R.E. Russo, Simulation of infrared picosecond laser-induced electron emission from semiconductors, Appl. Surf. Sci. 127–129 (1998) 206–211.
[41] J. Güdde, J. Hohlfeld, J.G. Müller, E. Matthias, Damage threshold dependence on electron–phonon coupling in Au and Ni films, Appl. Surf. Sci. 127–129 (1998) 40–45.
[42] J. Jandeleit, G. Urbasch, H.D. Hoffmann, H.-G. Treusch, E.W. Kretz, Picosecond laser ablation of thin copper films, Appl. Phys. A 63 (1996) 117–121.
[43] W.S. Fann, R. Storz, H.W.K. Tom, J. Bokor, Direct measurement of non-equilibrium electron energy distributions in subpicosecond laser-heated gold films, Phys. Rev. Lett. 68 (1992) 2834–2837.
[44] T. Juhasz, H.E. Elsayed-Ali, X.H. Hu, W.E. Bron, Time-resolved thermoreflectivity of thin gold films and its dependence on the ambient temperature, Phys. Rev. B 45 (1992) 13 819–13 822.
[45] H.E. Elsayed-Ali, T.B. Norris, M.A. Pessot, G.A. Mourou, Time-resolved observation of electron–phonon relaxation in copper, Phys. Rev. Lett. 58 (1987) 1212–1215.
[46] G.L. Eesley, Generation of non-equilibrium electron and lattice temperature in copper by picosecond laser pulses, Phys. Rev. B 33 (1986) 2144–2151.
[47] S.S. Wellershoff, J. Hohlfeld, J. Güdde, E. Matthias, The role of electron–phonon coupling in femtosecond laser damage of metals, Appl. Phys. A 69 (1999) S99–S107.
[48] T.Q. Qiu, C.L. Tien, Heat transfer mechanisms during short-pulse laser heating of metals, J. Heat Transfer 115 (1993) 835–841.
[49] E. Ohmura, I. Fukumoto, Molecular dynamics simulation of laser ablation of fcc metal, Int. J. Jpn. Soc. Prec. Eng. 30 (1996) 128–133.
[50] E. Ohmura, I. Fukumoto, I. Miyamoto, Molecular dynamics simulation of laser ablation of metal and silicon, Int. J. Jpn. Soc. Prec. Eng. 32 (1998) 248–253.
[51] X. Wu, M. Sadeghi, A. Vertes, Molecular dynamics of matrix assisted laser desorption of leucine enkephalin guest molecules from nicotinic acid host crystal, J. Phys. Chem. 102 (1998) 4770–4778.
[52] T.E. Itina, L.V. Zhigilei, B.J. Garrison, Microscopic mechanisms of matrix assisted laser desorption of analyte molecules: insights from molecular dynamics simulation, J. Phys. Chem. 106 (2002) 303–310.
[53] L.V. Zhigilei, B.J. Garrison, Microscopic mechanisms of laser ablation of organic solids in the thermal and stress confinement irradiation regimes, J. Appl. Phys. 88 (2000) 1281–1298.
[54] L.V. Zhigilei, E. Leveugle, B.J. Garrison, Y.G. Yingling, M.I. Zeifman, Computer simulations of laser ablation of molecular substrates, Chem. Rev. 103 (2003) 321–347.
[55] D. Perez, L.J. Lewis, Ablation of solids under femtosecond laser pulses, Phys. Rev. Lett. 89 (2002) 255 504.
[56] R.F. Haglund Jr., Microscopic and mesoscopic aspects of laser-induced desorption and ablation, Appl. Surf. Sci. 96–98 (1996) 1–13.
[57] A.M. Stoneham, M.M.D. Ramos, R.M. Ribeiro, The mesoscopic modeling of laser ablation, Appl. Phys. A 69 (1999) S81–S86.
[58] R. Mendes Ribeiro, M.M.D. Ramos, A.M. Stoneham, J.M. Correia Pires, Modeling of surface evaporation by laser ablation, Appl. Surf. Sci. 109–110 (1997) 158–161.
[59] R. MendesRibeiro, M.M.D. Ramos, A.M. Stoneham, Mesoscopic study of laser absorption by a transparent ceramic, Comp. Mater. Sci. 10 (1998) 33–37.
[60] N. Bityurin, N. Arnold, B. Luk'yanchuk, D. Bäuerle, Bulk model of laser ablation of polymers, Appl. Surf. Sci. 127–129 (1998) 164–170.
[61] N. Arnold, B. Luk'yanchuk, N. Bityurin, A fast quantitative modeling of ns laser ablation based on non-stationary averaging technique, Appl. Surf. Sci. 127–129 (1998) 184–192.
[62] J.G. Lunney, R. Jordan, Pulsed laser ablation of metals, Appl. Surf. Sci. 127–129 (1998) 941–946.
[63] A.D. Boardman, B. Cresswell, J. Anderson, An analytical model for the laser ablation of materials, Appl. Surf. Sci. 96–98 (1996) 55–60.
[64] S.I. Anisimov, N.A. Inogamov, A.M. Oparin, B. Rethfeld, T. Yabe, M. Ogawa, V.E. Fortov, Pulsed laser evaporation: equation-of-state effects, Appl. Phys. A 69 (1999) 617–620.
[65] S. Tosto, Assessment of the boundary conditions for a thermal model of pulsed laser ablation, J. Phys. D: Appl. Phys. 35 (2002) 770–778.
[66] D.I. Rosen, J. Mitteldorf, G. Kothandaraman, A.N. Pirri, E.R. Pugh, Coupling of pulsed 0.35 μm laser radiation to aluminum alloys, J. Appl. Phys. 53 (1982) 3190–3200.
[67] A. Vertes, P. Juhasz, M. De Wolf, R. Gijbels, Hydrodynamic modeling of laser plasma ionization processes, Int. J. Mass Spectrom. Ion Proc. 94 (1989) 63–85.
[68] A. Vertes, G. Irinyi, R. Gijbels, Hydrodynamic model of matrix-assisted laser desorption mass spectrometry, Anal. Chem. 65 (1993) 2389–2393.

[69] G. Colonna, A. Casavola, M. Capitelli, Modeling of LIBS plasma expansion, Spectrochim. Acta Part B 56 (2001) 567–586.
[70] A.V. Bulgakov, N.M. Bulgakova, Dynamics of laser-induced plume expansion into an ambient gas during film deposition, J. Phys. D: Appl. Phys. 28 (1995) 1710–1718.
[71] J.R. Ho, C.P. Grigoropoulos, J.A.C. Humphrey, Gas dynamics and radiation heat transfer in the vapor plume produced by pulsed laser irradiance of aluminum, J. Appl. Phys. 79 (1996) 7205–7215.
[72] J.N. Leboeuf, K.R. Chen, J.M. Donato, D.B. Geohegan, C.L. Liu, A.A. Puretzky, R.F. Wood, Modeling of plume dynamics in laser ablation processes for thin film deposition of materials, Phys. Plasmas 3 (1996) 2203–2209.
[73] R.F. Wood, K.R. Chen, J.N. Leboeuf, A.A. Puretzky, D.B. Geohegan, Dynamics of plume propagation and splitting during pulsed laser ablation, Phys. Rev. Lett. 79 (1997) 1571–1574.
[74] R.F. Wood, J.N. Leboeuf, K.R. Chen, D.B. Geohegan, A.A. Puretzky, Dynamics of plume propagation, splitting and nanoparticle formation during pulsed-laser ablation, Appl. Surf. Sci. 127–129 (1998) 151–158.
[75] A.V. Gusarov, A.G. Gnedovets, I. Smurov, Two-dimensional gas-dynamic model of laser ablation in an ambient gas, Appl. Surf. Sci. 154–155 (2000) 66–72.
[76] M. Capitelli, F. Capitelli, A. Eletskii, Non-equilibrium and equilibrium problems in laser-induced plasmas, Spectrochim. Acta Part B 55 (2000) 559–574.
[77] G. Callies, H. Schittenhelm, P. Berger, H. Hügel, Modeling of the expansion of laser-evaporated matter in argon, helium and nitrogen and the condensation of clusters, Appl. Surf. Sci. 127–129 (1998) 134–141.
[78] A.G. Gnedovets, A.V. Gusarov, I. Smurov, A model for nanoparticle synthesis by pulsed laser evaporation, J. Phys. D: Appl. Phys. 32 (1999) 2162–2168.
[79] A.G. Gnedovets, A.V. Gusarov, I. Smurov, Submicron particles synthesis by laser evaporation at low power density: a numerical analysis, Appl. Surf. Sci. 154–155 (2000) 508–513.
[80] A.V. Gusarov, A.G. Gnedovets, I. Smurov, G. Flamant, Simulation of nanoscale particles elaboration in laser-produced erosive flow, Appl. Surf. Sci. 154–155 (2000) 331–336.
[81] D. Blair, M. Tillack, M. Zaghloul, Prediction of particulate characteristics in an expanding laser plume, SPIE Conference on Micromachining and Microfabrication, San Francisco, CA, October 2001.
[82] T.E. Itina, W. Marine, M. Autric, Monte Carlo simulation of the effects of elastic collisions and chemical reactions on the angular distributions of the laser ablated particles, Appl. Surf. Sci. 127–129 (1998) 171–176.
[83] I. NoorBatcha, R.R. Lucchese, Y. Zeiri, Monte Carlo simulations of gas-phase collisions in rapid desorption of molecules from surfaces, J. Chem. Phys. 86 (1987) 5816–5824.
[84] F. Garrelie, J. Aubreton, A. Catherinot, MC simulation of the laser-induced plasma plume expansion under vacuum: comparison with experiment, J. Appl. Phys. 83 (1998) 5075–5082.
[85] D. Sibold, H.M. Urbassek, Effect of gas-phase collisions in pulsed-laser desorption: a three-dimensional Monte Carlo simulation study, J. Appl. Phys. 73 (1993) 8544–8551.
[86] T.E. Itina, V.N. Tokarev, W. Marine, M. Autric, Monte Carlo simulation study of the effects of non-equilibrium chemical reactions during pulsed laser desorption, J. Chem. Phys. 106 (1997) 8905–8912.
[87] O. Ellegaard, J. Schou, H.M. Urbassek, Monte Carlo description of gas flow from laser-evaporated silver, Appl. Phys. A 69 (1999) S577–S581.
[88] F. Garrelie, C. Champeaux, A. Catherinot, Study by a Monte Carlo simulation of the influence of a background gas on the expansion dynamics of a laser-induced plasma plume, Appl. Phys. A 69 (1999) 45–50.
[89] J.C.S. Kools, Monte Carlo simulations of the transport of laser-ablated atoms in a diluted gas, J. Appl. Phys. 74 (1993) 6401–6406.
[90] F. Garrelie, C. Champeaux, A. Catherinot, Expansion dynamics of the plasma plume created by laser ablation in a background gas, Appl. Phys. A 69 (1999) S55–S58.
[91] T.E. Itina, L. Patrone, W. Marine, M. Autric, Numerical analysis of TOF measurements in pulsed laser ablation, Appl. Phys. A 69 (1999) S59–S65.
[92] M. Han, Y. Gong, J. Zhou, C. Yin, F. Song, N. Muto, T. Takiya, Y. Iwata, Plume dynamics during film and nanoparticles deposition by pulsed laser ablation, Phys. Lett. A 302 (2002) 182–189.
[93] T.E. Itina, J. Hermann, Ph. Delaporte, M. Sentis, Laser-generated plasma plume expansion: combined continuous-microscopic modeling, Phys. Rev. E 66 (2002) 066 406.
[94] T.E. Itina, J. Hermann, Ph. Delaporte, M. Sentis, Combined continuous-microscopic modeling of laser plume expansion, Appl. Surf. Sci. 208–209 (2003) 27–32.
[95] X. Mao, R.E. Russo, Observation of plasma shielding by measuring transmitted and reflected laser pulse temporal profiles, Appl. Phys. A 64 (1997) 1–6.
[96] G. Colonna, L.D. Pietanza, M. Capitelli, Coupled solution of a time-dependent collisional-radiative model and Boltzmann equation for atomic hydrogen plasmas: possible implications with LIBS plasmas, Spectrochim. Acta Part B 56 (2001) 587–598.
[97] S.S. Mao, X. Mao, R. Greif, R.E. Russo, Initiation of an early-stage plasma during picosecond laser ablation of solids, Appl. Phys. Lett. 77 (2000) 2464–2466.
[98] X.L. Mao, W.T. Chan, M.A. Shannon, R.E. Russo, Plasma shielding during picosecond laser sampling of solid materials by ablation in He vs. Ar atmosphere, J. Appl. Phys. 74 (1993) 4915–4922.
[99] S.S. Mao, X. Mao, R. Greif, R.E. Russo, Simulation of a picosecond laser ablation plasma, Appl. Phys. Lett. 76 (2000) 3370–3372.

[100] R. Hedwig, T.J. Lie, M.O. Tjia, K. Kagawa, H. Kurniawan, Confinement effect in enhancing shock wave plasma generation at low pressure by TEA $CO_2$ laser bombardment on quartz sample, Spectrochim. Acta Part B 58 (2003) 531–542.

[101] V. Margetic, T. Ban, F. Leis, K. Niemax, R. Hergenröder, Hydrodynamic expansion of a femtosecond laser produced plasma, Spectrochim. Acta Part B 58 (2003) 415–425.

[102] S.S. Harilal, C.V. Bindhu, M.S. Tillack, F. Najmabadi, A.C. Gaeris, Internal structure and expansion dynamics of laser ablation plumes into ambient gases, J. Appl. Phys. 93 (2003) 2380–2388.

[103] W.T. Chan, A.P.K. Leung, X.L. Mao, R.E. Russo, Effects of gas environment on picosecond laser ablation, Appl. Surf. Sci. 127–129 (1998) 269–273.

[104] A.P.K. Leung, W.T. Chan, X.L. Mao, R.E. Russo, Influence of gas environment on picosecond laser ablation sampling efficiency and ICP conditions, Anal. Chem. 70 (1998) 4709–4716.

[105] S.H. Jeong, O.V. Borisov, J.H. Yoo, X.L. Mao, R.E. Russo, Effects of particle size distribution on inductively coupled plasma mass spectrometry signal intensity during laser ablation on glass samples, Anal. Chem. 71 (1999) 5123–5130.

[106] M. Guillong, D. Günther, Effect of particle size distribution on ICP-induced elemental fractionation in laser ablation inductively coupled plasma mass spectrometry, J. Anal. At. Spectrom. 17 (2002) 831–837.

[107] I. Rodushkin, M.D. Axelsson, D. Malinovsky, D.C. Baxter, Analyte- and matrix-dependent elemental response variations in laser ablation inductively coupled plasma mass spectrometry, J. Anal. At. Spectrom. 17 (2002) 1223–1230.

[108] M. Guillong, H.-R. Kuhn, D. Günther, Application of a particle separation device to reduce inductively coupled plasma-enhanced elemental fractionation in laser ablation inductively coupled plasma mass spectrometry, Spectrochim. Acta Part B 58 (2003) 211–220.

[109] S.E. Jackson, D. Günther, The nature and sources of laser-induced isotopic fractionation in laser ablation multicollector inductively coupled plasma mass spectrometry, J. Anal. At. Spectrom. 18 (2003) 205–212.

[110] H.-R. Kuhn, D. Günther, Elemental fractionation studies in laser ablation inductively coupled plasma mass spectrometry on laser-induced brass aerosols, Anal. Chem. 75 (2003) 747–753.

[111] H. Schittenhelm, G. Callies, P. Berger, H. Hügel, Investigations of extinction coefficients during excimer laser ablation and their interpretation in terms of Rayleigh scattering, J. Phys. D: Appl. Phys. 29 (1996) 1564–1575.

[112] K. Suizu, K. Nagayama, Cooling of pulsed laser-ablated plasma plume in an ambient gas and the onset condition of clustering in nanoparticle synthesis, Appl. Phys. A 69 (1999) S235–S238.

[113] H.W. Kroto, J.R. Heath, S.C. O'Brien, R.F. Curl, R.E. Smalley, $C_{60}$: Buckminsterfullerene, Lett. Nat. 138 (1985) 162–163.

[114] D.B. Geohegan, A.A. Puretzky, G. Duscher, S.J. Pennycook, Photoluminescence from gas-suspended $SiO_x$ nanoparticles synthesized by laser ablation, Appl. Phys. Lett. 73 (1998) 438–440.

[115] W. Marine, L. Patrone, B. Luk'yanchuk, M. Sentis, Strategy of nanocluster and nanostructure synthesis by conventional pulsed laser ablation, Appl. Surf. Sci. 154–155 (2000) 345–352.

[116] R. Stewart, L. Li, R. Isherwood, Rapid vaporization mechanism in enclosed laser ablation, J. Phys. D: Appl. Phys. 36 (2003) 303–310.

[117] L.V. Zhigilei, Dynamics of the plume formation and parameters of the ejected clusters in short-pulse laser ablation, Appl. Phys. A 76 (2003) 339–350.

[118] A.B. Brailovsky, S.V. Gaponov, V.I. Luchin, Mechanisms of melt droplets and solid particle ejection from a target surface by pulsed laser action, Appl. Phys. A 61 (1995) 81–86.

[119] D.E. Hare, J. Franken, D.D. Dlott, Coherent Raman measurements of polymer thin-film pressure and temperature during picosecond laser ablation, J. Appl. Phys. 77 (1995) 5950–5960.

[120] A.A. Oraevsky, S.L. Jacques, F.K. Tittel, Mechanisms of laser ablation for aqueous media irradiated under confined-stress conditions, J. Appl. Phys. 78 (1995) 1281–1290.

[121] D. Günther, Private communication.

[122] T.D. Bennett, C.P. Grigoropoulos, D.J. Krajnovich, Near-threshold laser sputtering of gold, J. Appl. Phys. 77 (1995) 849–864.

[123] X. Zhang, S.S. Chu, J.R. Ho, C.P. Grigoropoulos, Excimer laser ablation of thin gold films on a quartz crystal microbalance at various argon background pressures, Appl. Phys. A 64 (1997) 545–552.

[124] J.H. Yoo, S.H. Jeong, X.L. Mao, R. Greif, R.E. Russo, Evidence for phase-explosion and generation of large particles during high power nanosecond laser ablation of silicon, Appl. Phys. Lett. 77 (2000) 783–785.

[125] J.H. Yoo, S.H. Jeong, R. Greif, R.E. Russo, Explosive change in crater properties during high power nanosecond laser ablation of silicon, J. Appl. Phys. 88 (2000) 1638–1649.

[126] Q. Lu, S.S. Mao, X. Mao, R.E. Russo, Delayed phase explosion during high-power nanosecond laser ablation of silicon, Appl. Phys. Lett. 80 (2002) 3072–3074.

[127] Q. Lu, Thermodynamic evolution of phase explosion during high-power nanosecond laser ablation, Phys. Rev. E 67 (2003) 016 410.

[128] Z. Chen, A. Bogaerts, R. Gijbels, Paper in preparation.

[129] J.A. McMordie, P.D. Roberts, The interaction of pulsed $CO_2$ laser radiation with aluminium, J. Phys. D: Appl. Phys. 8 (1975) 768–781.

[130] C.T. Walters, A.H. Clauer, Transient reflectivity behavior of pure aluminium at 10.6 μm, Appl. Phys. Lett. 33 (1978) (1978) 713–715.
[131] P. Atkins, J. dePaula, Atkins' Physical Chemistry, 7th ed, Oxford University Press, Oxford, 2002.
[132] R. Kelly, On the dual role of the Knudsen layer and unsteady, adiabatic expansion in pulse sputtering phenomena, J. Chem. Phys. 92 (1990) 5047–5056.
[133] D.R. Lide, CRC Handbook of Chemistry and Physics, 83rd ed, CRC Press, Boca Raton, 2002–2003.
[134] L. Spitzer, Physics of Fully Ionized Gases, Interscience Publishers, London, 1956.
[135] S.K. Godunov, Raznostniy metod chislennogo rascheta razrivnih resheniy uravneniy gidrodinamiki (paper in Russian; English translation: Difference method of the numerical calculation of discontinuous solutions of the equations of hydrodynamics), Matemat. Sborn. 47 (1959) 271–306.
[136] S.K. Godunov, A.V. Zabrodin, G.P. Prokopov, Raznostnaya skhema dlya dvukhmernikh nestatcionarnih zadach gazovoy dinamiki i raschet o btekaniya s otoshedshey udarnoy volnoy (paper in Russian; English translation: Differential scheme for 2D non-stationary problems of gas dynamics and modeling of shock waves), USSR Comput. Math. Math. Phys. 6 (1961) 1020–1050.
[137] J.D. Anderson, Computational Fluid Dynamics, McGrawHill, New York, 1995.
[138] R.D. Richtmyer, K.W. Morton, Finite Difference Methods for Initial Value Problems, Wiley, New York, 1967.
[139] C. Hirsch, Numerical computation of internal and external flows, Computational Methods for Inviscid and Viscous Flows, 2,, Wiley, Chichester, 1990.
[140] R.L. Burden, J.D. Faires, A.C. Reynolds (Eds.), Numerical Analysis, Prindle, Weber and Schmidt, Boston, 1978.
[141] J.F. Ready, Mechanism of electron emission produced by a giant-pulse laser, Phys. Rev. 137 (1965) A620–A623.
[142] E.M. Logothetis, P.L. Hartman, Laser-induced electron emission from solids: many-photon photoelectric effects and thermionic emission, Phys. Rev. 187 (1969) 460–474.
[143] S.I. Anisimov, B.L. Kapeliovich, T.L. Perel'man, Electron emission from metal surfaces exposed to ultrashort laser pulses, Sov. Phys.-JETP 39 (1974) 375–377.
[144] H.C. Liu, X.L. Mao, J.H. Yoo, R.E. Russo, Early phase laser-induced plasma diagnostics and mass removal during single-pulse laser ablation of silicon, Spectrochim. Acta Part B 54 (1999) 1607–1624.
[145] L.A. Doyle, G.W. Martin, A. Al-Khateeb, I. Weaver, D. Riley, M.J. Lamb, T. Morrow, C.L.S. Lewis, Electron number density measurements in magnesium laser produced plumes, Appl. Surf. Sci. 127–129 (1998) 716–720.
[146] G. Abdellatif, H. Imam, A study of the laser plasma parameters at different laser wavelengths, Spectrochim. Acta Part B 57 (2002) 1155–1165.
[147] E.M. Monge, C. Aragón, J.A. Aguilera, Space- and time-resolved measurements of temperatures and electron densities of plasmas formed during laser ablation of metallic samples, Appl. Phys. A 69 (1999) S691–S694.
[148] M.A. Hafez, M.A. Khedr, F.F. Elaksher, Y.E. Gamal, Characteristics of Cu plasma produced by a laser interaction with a solid target, Plasma Sources Sci. Technol. 12 (2003) 185–198.
[149] J. Hermann, C. Vivien, A.P. Carricato, C. Boulmer-Leborgne, A spectroscopic study of laser ablation plasmas from Ti, Al and C targets, Appl. Surf. Sci. 127–129 (1998) 645–649.
[150] R.W. Dreyfus, $Cu^0$, $Cu^+$ and $Cu_2$ from excimer-ablated copper, J. Appl. Phys. 69 (1991) 1721–1729.
[151] S. Amoruso, V. Berardi, R. Bruzzese, N. Spinelli, X. Wang, Kinetic energy distribution of ions in the laser ablation of copper targets, Appl. Surf. Sci. 127–129 (1998) 953–958.
[152] S. Amoruso, M. Armenante, V. Berardi, R. Bruzzese, R. Velotta, X. Wang, High fluence visible and ultraviolet laser ablation of metallic targets, Appl. Surf. Sci. 127–129 (1998) 1017–1022.
[153] Y. Franghiadakis, C. Fotakis, P. Tzanetakis, Energy distribution of ions produced by excimer-laser ablation of solid and molten targets, Appl. Phys. A 68 (1999) 391–397.
[154] M.A. Shannon, X.L. Mao, A. Fernandez, W.-T. Chan, R.E. Russo, Laser ablation mass removal vs. incident power density during solid sampling for inductively coupled plasma atomic emission spectroscopy, Anal. Chem. 67 (1995) 4522–4529.